J. Fluid Mech. (1995), *vol.* 285, *pp.* 371-406
Copyright © 1995 Cambridge University Press

The effects of a vertical contraction on turbulence dynamics in a stably stratified fluid

By S.T. THORODDSEN† AND C.W. VAN ATTA‡

Applied Mechanics and Engineering Sciences, University of California, San Diego, La Jolla, CA 92093-0411, USA

(Received 21 April 1993 and in revised form 23 September 1994)

We have experimentally studied the effects of mean strain on the evolution of stably stratified turbulence. Grid-generated turbulence ($Re_\lambda \leqslant 25$) in a stable linear mean background density gradient was passed through a two-dimensional contraction, contracting the stream only in the vertical direction. This induces an increase in stratification strength, which reduces the largest vertical overturning scales allowed by buoyancy forces. The mean strain through the contraction causes, on the other hand, stretching of streamwise vortices tending to increase the fluctuation levels of the transverse velocity components. This competition between buoyancy and vortex stretching dominates the turbulence dynamics inside and downstream of the contraction. Comparison between non-stratified and stratified experiments shows that the stratification significantly reduces the vertical velocity fluctuations. The vertical heat flux is initially enhanced through the contraction. Then, farther downstream the flux quickly reverses, leading to very strong restratification coinciding with an increase in the vertical velocity fluctuations. The vertical heat flux collapses much more rapidly than in the stratified case without an upstream contraction and the restratification intensity is also much stronger, showing values of normalized flux as strong as -0.55. Velocity spectra show that the revival of vertical velocity fluctuations, due to the strong restratification, starts at the very largest scales but is then subsequently transferred to smaller scales. The distance from the turbulence-generating grid to the entrance of the contraction is an important parameter which was varied in the experiments. The larger this distance, the larger the integral length scale can grow, approaching the limit set by buoyancy, before entering the contraction. The evolution of the various turbulence length scales is described. Two-point measurements of velocity and temperature transverse integral scales were also performed inside the contraction. The emergence of 'zombie' turbulence, for large buoyancy times, is in good quantitative agreement with the numerical simulations of Gerz & Yamazaki (1993) for stratification number larger than 1.

---

† Present address: Department of Theoretical and Applied Mechanics, University of Illinois at Urbana-Champaign, Urbana IL 61801-2935, USA.

‡ Also Scripps Institution of Oceanography.

1. Introduction

The situation sometimes arises in geophysical flows in the ocean and atmosphere that turbulent fluid enters or evolves in a stably stratified environment with a spatially varying stratification strength. This occurs for example when ocean surface water cools at night through surface radiative heat loss and then sinks into stongly stratified inversions at depth. Other examples include convergence of isopycnals by internal waves, which introduces spatial and temporal variation in the stratification strength, and tongues of ocean currents entering fluid masses of varying density stratifications as rivers issue into the saline abyss. Flow over sills and through strait topography also causes convergence of isopycnals. The hydrodynamics of exchange layers in the Gibraltar Strait have been studied by Armi & Farmer (1986) and Farmer & Armi (1986) and the rich variety of dynamical character observed in some cases gives rise to turbulence under conditions of varying stratification.

To study these effects of spatially varying stratification strength on evolving turbulence, we have passed a linearly stratified turbulent field through a contraction in the vertical direction. The contraction confines the flow in a narrower vertical extent, thus increasing the stratification strength, but at the same time it increases the transverse velocity fluctuations due to the stretching of streamwise vortices. The competition between the stabilizing buoyancy and overturning inertial vortex forces will thus determine the dynamical evolution of the turbulence. Owing to these complicated dynamics inside the contraction, one can expect the turbulence downstream of the contraction to evolve under dynamic conditions not encountered in decaying grid turbulence without a contraction.

The evolution of the scalar field in the present experiments is of particular interest regarding the formation and existence of 'fossil' scalar fluctuations. The main premise of 'fossil' turbulence is stated by Gibson (1980, p. 225):

> The physical process leading to fossil turbulence is that buoyancy forces remove turbulent kinetic energy at large scales, but no comparable mechanism removes the large scale fluctuations of scalar fluid properties, such as temperature, produced by the original turbulence.

One may therefore expect significant fossil turbulence to exist after the contraction where N has increased suddenly and fluid parcels producing density fluctuations suddenly find themselves far out of their equilibrium locations.

We have not been able to find any previous experimental work on this problem, not even for the passively stratified mean gradient case.

The decay of grid-generated turbulence in a stably stratified fluid was studied initially in tow-tanks by Lin & Veenhuizen (1975), Dickey & Mellor (1980) and Britter *et al.* (1983), then in salt-stratified water channels by Stillinger, Helland & Van Atta (1983) and Itsweire, Helland & Van Atta (1986) and most recently in thermally stratified wind tunnels by Lienhard & Van Atta (1990) and Yoon & Warhaft (1990). Thoroddsen & Van Atta (1992, 1993*a*,*b*) have further studied the development of small-scale anisotropy due to buoyancy and the effects of grid configuration on the turbulence evolution. Rohr *et al.* (1988) have included the effects of mean velocity shear in their stratified water facility.

Prandtl (1933) first argued that as a contraction accelerates the fluid passing through it, the streamwise vortex filaments are stretched and the transverse velocity fluctuations are increased. Conversely, the vertically oriented vortex filaments are compressed, reducing the streamwise velocity fluctuations. This is one of the principles used in the design of wind tunnels to lower the background turbulence intensity. For a graphical illustration see Tennekes & Lumley (1972, p. 83).

The seminal experimental work on the effects of the straining of turbulence without stratification is due to Townsend (1954). Since then numerous authors have studied the effects of uniform strain on turbulence by passing the turbulent field through a contraction, but studies including the straining of a turbulent scalar field are few. Studies of the effects of a contraction on passive non-stratified turbulent scalar fields are due to Mills & Corrsin (1959) and Warhaft (1980). The most significant difference between passively stratified and non-stratified studies is that without the mean gradient of the scalar there is a lack of generation of new scalar fluctuations due to movement of fluid elements against this mean gradient. In the non-stratified case the scalar fluctuations diminish therefore monotonically away from their point of inception, usually at a heated grid. The decay of scalar fluctuations generated by heated grids have been studied extensively by Mills *et al.* (1958), Yeh & Van Atta (1973) and others, as reviewed by Warhaft & Lumley (1978). For the stratified cases studied here, not only are new scalar fluctuations generated by the movement of fluid elements against the mean gradient, but the scalar is also strongly active, i.e. directly affects the velocity field, through the buoyancy forces.

Recent DNS have been performed by Gerz & Yamazaki (1993), where turbulence is generated from initially stationary frozen density fluctuations residing in a background mean gradient of density. The vigour of the resulting turbulent flow field, called 'zombie' turbulence by Gerz & Yamazaki, was found to be characterized by the initial 'stratification number',

$$St_o = \frac{\Lambda_\theta}{\theta_o}\frac{\mathrm{d}T}{\mathrm{d}z}, \tag{1.1}$$

where Λ_θ is the integral length scale of the density field and θ_o the initial intensity of density fluctuations. Initial stratification numbers less than 1 gave rise to turbulence with strong nonlinear transfer and mixing, whereas St_o of unity or larger led to a more linear type of motion of vertically oscillating blobs of fluid. In the last section of this paper some of our results are compared to these DNS.

Batchelor, Canuto & Chasnov (1992) have performed similar large-eddy simulations (LES), but in a fluid with no background mean density gradient. In this situation the buoyancy starts the motion and generates turbulent interactions, which evolve and eventually self-destruct by the induced stirring and mixing of the scalar, whose variation introduced the buoyancy forces driving the motion. They define a pseudo-Reynolds number as

$$R = \frac{(g\theta_o \Lambda_\theta^3)^{1/2}}{\nu} \tag{1.2}$$

where θ_o is dimensionless. They observe that the evolution time from rest to maximum turbulent activity becomes independent of this Reynolds number for sufficiently high values of R. Chasnov (1991) has extended this work to decaying turbulence in a passive mean scalar gradient. In the present work we have investigated the effects of Re_λ (defined in §2) by using different grid mesh sizes.

The following section introduces various length scales and terminology used in the study of stratified turbulence. Section 3 describes the experimental setup and instrumentation, followed by experimental results in §4. Finally §5 reviews and discusses the main results along with comparison with some numerical simulation results.

2. Turbulent scale evolution in stratified turbulence

In this section we will introduce the important turbulence length scales which are derived from the relative strength of the forces of inertia, buoyancy and viscosity. We will also discuss the effects of the contraction on these length scales.

In very broad terms the evolution of stably stratified decaying turbulence is the following: the turbulent kinetic energy is dissipated by viscosity and the turbulent integral length scale grows until it becomes limited in the vertical by buoyancy forces. This has been demonstrated, e.g. by Itsweire *et al.* (1986) in a salt-stratified water tunnel, as well as in thermally stratified wind tunnels by Lienhard & Van Atta (1990) and Yoon & Warhaft (1990). The conventional definitions of the relevant length scales are presented in these publications and will only be briefly reviewed here. We follow the nomenclature of Lienhard & Van Atta (1990).

The stratification strength is characterized by the Brunt-Väisälä frequency,

$$N = \left(-\frac{g}{\rho_o}\frac{\mathrm{d}\rho}{\mathrm{d}z}\right)^{1/2} = \left(\frac{g}{T_o}\frac{\mathrm{d}T}{\mathrm{d}z}\right)^{1/2} \tag{2.1}$$

and has the units of rad s^{-1}. It is the frequency of oscillation of a fluid element displaced in the vertical direction, away from its neutral density position.

The buoyancy length scale is defined as

$$L_b = \frac{w}{N} \tag{2.2}$$

and denotes the r.m.s. vertical distance a fluid element can travel in converting all its vertical kinetic energy into potential energy. This upper bound of vertical motion is also often estimated in terms of the Ozmidov scale which is obtained by equating the buoyancy and inertial forces,

$$L_O = \left(\frac{\epsilon}{N^3}\right)^{1/2}, \tag{2.3}$$

where ϵ is the viscous dissipation rate per unit mass. The assumptions used in deriving this expression ($w\ell/N \approx 1$ and $\epsilon = w^3/\ell$, Ozmidov 1965) are probably not applicable to the conditions inside the contraction, but this scale can still be used as a reference.

The overturning scale is often used to characterize the length scale of the actively turbulent eddies:

$$L_t = \frac{\theta}{\mathrm{d}T/\mathrm{d}z}. \tag{2.4}$$

The definition of L_t is based on the implicit assumption that the turbulent field is in a local equilibrium state, i.e. the turbulent motions generate the temperature fluctuations by moving the fluid elements against a background mean gradient and are not simply remnants of a previous turbulent state, i.e. fossil temperature. In our case $\mathrm{d}T/\mathrm{d}z$ is rapidly changing through the contraction and directional isotropy of the flow field is also not valid so that the integral scales of motion in the vertical and horizontal directions are generally no longer equal.

The overturning scale in non-stratified turbulence is commonly characterized by ℓ:

$$\ell = \frac{u^3}{\epsilon}. \tag{2.5}$$

The smallest scale of turbulent motion is the Kolmogorov microscale,

$$\eta = \left(\frac{\nu^3}{\epsilon}\right)^{1/4} \tag{2.6}$$

and the corresponding microscale for the scalar is the Batchelor scale,

$$\eta_\theta = \left(\frac{\alpha^3}{\epsilon}\right)^{1/4} = \eta Pr^{-3/4} \tag{2.7}$$

where ν and α are respectively the kinematic viscosity and the thermal diffusivity. This relation is valid for Prandtl number $Pr = \nu/\alpha$ of the order of 1.

The Reynolds number used herein is $Re_\lambda = u'\lambda/\nu$ based on the Taylor microscale $\lambda^2 = \overline{u^2}/\overline{(\partial u/\partial x)^2}$.

The turbulent energy balance most important to stably stratified flows describes the exchange between potential and vertical kinetic energy. The vertical turbulent kinetic energy of the fluid per unit volume is

$$\overline{T}_w = \tfrac{1}{2}\rho_0 \overline{w^2} \tag{2.8}$$

and the corresponding r.m.s. potential energy is in turn

$$\overline{\Psi} = \tfrac{1}{2}\rho_0 N^2 L_t^2. \tag{2.9}$$

From (2.2) and (2.4) it is clear that

$$\frac{\overline{T_w}}{\overline{\Psi}} = \left(\frac{L_b}{L_t}\right)^2. \tag{2.10}$$

The total turbulent kinetic energy per unit volume is $\overline{T} = \frac{1}{2}\rho q^2$, where $q^2 = \overline{u^2} + \overline{v^2} + \overline{w^2}$.

The total fluctuation energy per unit volume is therefore $\overline{T} + \overline{\Psi}$ for which the balance equation is

$$\frac{\mathrm{D}}{\mathrm{D}t}(\overline{T} + \overline{\Psi}) = \epsilon + \chi. \tag{2.11}$$

Buoyancy flux transfers of opposite sign in the individual component equations for $\overline{T}$ and $\overline{\Psi}$ can transfer energy back and forth between $\overline{T}$ and $\overline{\Psi}$, while the total energy remains constant, except for irreversible losses to ϵ and χ, the rate of destruction of $\overline{\theta^2}$.

The aim of this study is to investigate the effects of spatially varying stratification strength on these various turbulent length scales and fluxes. The contraction imposes a mean strain as well as increasing the stratification strength. We now discuss how these imposed constraints might affect the evolution or meaning of these scales.

First we demonstrate that our specific contraction is not 'sudden'. It extends 0.76 m in the streamwise direction. This corresponds to an actual dimensional travel time t of 0.54 s, obtained by integrating the local mean velocity through the contraction,

$$t = \int_{x_1}^{x_2} \frac{\mathrm{d}x^*}{U(x^*)}. \tag{2.12}$$

This corresponds to roughly one half of an overturning time scale, giving the turbulence some time to react to the local strain, before exiting the contraction. This is however not enough time for total adjustment of the mixing scalar field, as shown by Broadwell & Breidenthal (1982).

In an attempt to similarly account for the variation in $N(x)$ as well as $U(x)$ we also evaluated the non-dimensional *buoyancy evolution time* which integrates the effective stratification strength experienced by a fluid element,

$$\tau_N(x) = \int_0^x \frac{N(x^*)}{U(x^*)} \mathrm{d}x^*, \tag{2.13}$$

which gives a value of τ_N of 0.88 rad for the stronger stratification strength, N_2 = 2.22 rad s^{-1}. For grid turbulence without a contraction, where $N(x)$ and $U(x)$ are constants, Lienhard & Van Atta (1990) clearly demonstrated the collapse of the normalized buoyancy flux evolution curves with Nt scaling, where $t = x/U$ is the travel time from the grid. For these experiments the inhibition of vertical flux by buoyancy forces is complete at a downstream distance from the grid where $Nt \approx \pi$. Yoon & Warhaft (1990) subsequently proposed that internal Froude number scaling worked better to collapse data from different researchers. This scaling has been applied to laboratory and oceanographic data by Ivey & Imberger (1991). However, for the contracting case studied here there are difficulties associated with applying these types of time scalings, primarily since the turbulence gets restructured by the contraction and it is therefore not wise to start the evolution time at the grid. Owing to these ambiguities we have not applied buoyancy time scaling to many of the results presented in this paper.

From (2.3) it can be deduced that L_O will decrease through the contraction by $r^{-3/4}$, where r is the contraction ratio. For our contraction ratio (r = 2.5) this represents a reduction in L_O by one half. This rapid reduction in the Ozmidov scale will prohibit the overturning scale from growing, if L_t is of the order of L_O upstream.

We can also try to predict the changes in L_b due to the contraction. The contraction will increase both N as well as w', due to the stretching of streamwise vorticity. Looking at previous experimental non-stratified contraction data (Warhaft 1980, figure 2), for changes in w', one can predict a decrease in L_b of about 20%, but there may be a conceptual flaw in this estimate of the increase in L_b, based on the increase in w', if higher w' entails a smaller transverse integral length scale due to the stretching of the streamwise vortex filaments.

The above estimates of the reduction in the buoyancy length scales L_b and L_O by the contraction is *a priori* quite uncertain, i.e. the former should decrease by approximately 20% and the latter by 50%.

In the non-contraction experiments for decaying stratified turbulence L_t does not overtake L_O, so one may expect especially interesting physics to occur when the ratio L_t/L_O is close to or larger than 1/2 as the turbulence enters the contraction.

As discussed above, the changes in the buoyancy length scales in response to the contraction are unclear and the assumptions behind their definitions may break down. Some of this work has thus focused on clarifying this issue.

The evolution of the integral length scales due to the mean strain has been studied by Warhaft (1980). By looking at the peak in the one-dimensional velocity spectra, $E_{uu}(k_1)$ and $E_{ww}(k_1)$, Warhaft reached the following conclusion (which we paraphrase in current variables) about the changes in the directional length scales due to the contraction: *Thus the geometrical effect of the contraction is only slightly felt by the u component while for the w component the length scale is increased by the contraction ratio.* For the contracting case one can of course not associate the transverse length scales with the spectra measured in the streamwise direction. To clarify this ambiguity we have studied, by a separate set of experiments, the spatial correlation

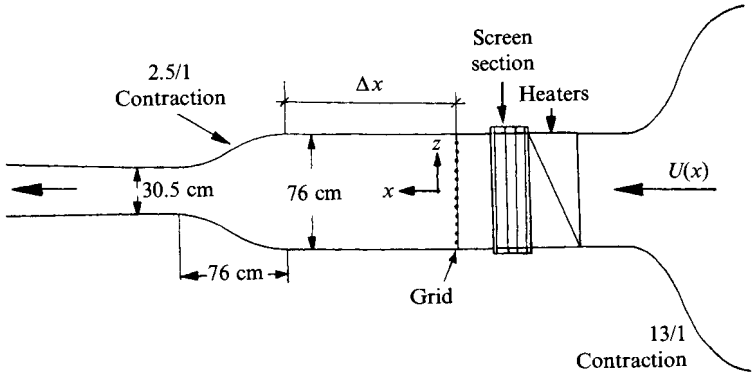

FIGURE 1. The wind-tunnel setup used to contract stably stratified grid-generated turbulence in the vertical direction. The horizontal width of the tunnel test section remains constant at 57.8 cm. Two different lengths Δx (48.3 and 101.6 cm) were used in the experiments.

of streamwise velocity in both the x- and z-directions to see more clearly how the transverse turbulent spatial scales react to the contraction.

We performed similar experiments for the temperture field. Assuming that the temperature field experiences a simple static stretching, similar to a rubber sheet, one can show that the length scale in the vertical direction will decrease by the strain ratio, while the streamwise scale will increase by the strain ratio. The ratio Λ_z/Λ_x will thus scale as r^{-2} for such simple stretching. The turbulent nonlinear interactions will, on the other hand, not allow a simple stretching of the turbulent velocity field, whose evolution will determine how the density length scales adjust themselves. The transverse integral scale of the temperature field inside the contraction was therefore studied by two-point cold-wire measurements, with the wires spaced in the vertical direction.

3. Experimental setup

3.1. *Wind tunnel and contraction*

The thermally stratified wind tunnel described in Lienhard & Van Atta (1989, 1990) was used for the experiments. The wind-tunnel setup was modified to allow for passing grid-generated turbulence through a contraction, as shown in figure 1. The coordinate system used here is the following: the x-axis is in the streamwise direction starting at the grid, with z pointing up in the vertical and y in the transverse direction. The air-flow upstream of the contraction has a linear mean temperature profile in the vertical direction. The flow is passed through a bi-planar grid to generate the turbulence which is subsequently advected through the contraction. The length Δx of the straight section extending between the grid and the start of the contraction is variable, allowing for different initial evolution times of the turbulence before contraction. This allows us to study turbulence with different ratios of overturning to buoyancy scales as it enters the contraction. The data presented here were collected for two different distances, i.e. Δx of 48.3 and 101.6 cm.

The contraction itself extended 76.2 cm in the streamwise direction. The contraction curve was formed by two circular arcs 69 cm in radius, and contracted the flow only in the vertical direction, leaving the tunnel width unchanged. The sides had double walls to divert cooler fluid coming from the ends of the heater assembly. The contraction

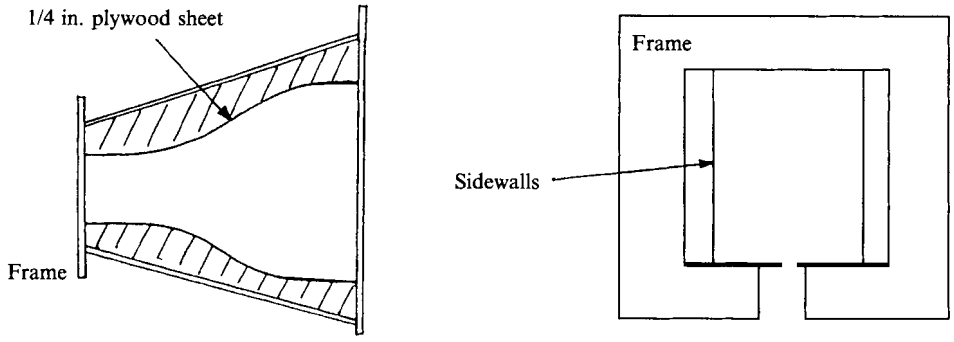

FIGURE 2. Schematic of the design of the contraction. It allows for traversing the measurement probes through the contraction itself, through a slot in the test-section floor. Sidewalls were added inside the test section to remove cooler boundary layers from the walls.

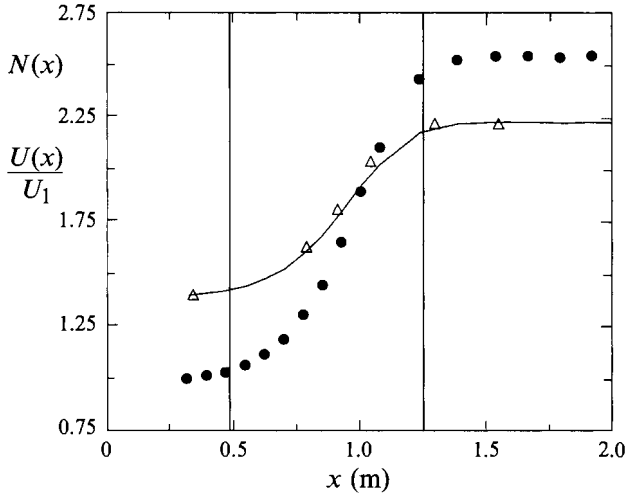

FIGURE 3. Mean velocity (•) on the centreline through the contraction normalized by the upstream mean velocity. Changes in the Brunt–Väisälä frequency through the contraction, obtained from measured vertical temperature profiles (△) and the corresponding values predicted from the geometric relations of equation (3.1) (—).

ratio was 2.5/1. The contraction was built with a slot running through its floor to allow for traversing the probes, to measure changes in turbulent quantities, inside the contracting zone. Figure 2 shows the design of the contraction and figure 3 shows the measured mean velocity through it. The maximum streamwise strain rate dU/dx through the contraction was 2.1 s^{-1} for the stratified runs and it persisted at approximately a constant rate for about 0.5 m in the streamwise direction, as is shown in figure 3.

3.2. *Stratification*

The heating was accomplished with an adjustable electric heater. It consisted of numerous thin metal plates (fins) aligned with the flow. These plates had 45 Calrods sticking through them in the spanwise direction. The rods were wired in 20 different sets, which could be adjusted individually with Variacs so as to attain a linear mean temperature profile and hence a constant gradient in the vertical direction.

The mean speed upstream of the contraction had to be kept low because it was limited by the constraint of allowing the heaters to generate the linear temperature profile in the vertical direction. If the tunnel was run at a higher velocity the profile would develop bumps at the locations of the heating rods, since the heat would not have time to conduct evenly into the heating fins before entering the flow. Downstream the mean velocity was $U_2 = 2.1$ m s^{-1} for the strongly stratified runs and 2.6 m s^{-1} for the weaker stratification. This resulted in rather low turbulent Reynolds numbers ($Re_\lambda < 25$). To study the dependence of the statistics on the turbulent Reynolds number, we used two different grid mesh sizes, i.e. $M = 2.54$ and 5.08 cm. The grids were biplanar and made out of round aluminium rods. The grid solidity was 34%.

The temperature boundary conditions were controlled by the heating Variacs and it was decided to keep the temperature profile upstream of the contraction linear and then let the flow itself select the vertical profiles through the contraction and into the downstream test section. The stratification strength increases through the contraction due to the increased vertical temperature gradient as the flow is confined in a shorter vertical extent. Figure 4 shows the mean vertical temperature profiles at streamwise locations upstream and downstream as well as inside the contraction. At the exit of the contraction the temperature profile developed a slightly S-shaped curve, as shown in the figure. The local N-values used here were determined from the approximately 20 cm centre parts of the vertical profiles, which are sufficiently wide in the vertical direction to completely control the turbulence dynamics on the centreline. Figure 3 shows the N-values corresponding to the temperature profiles in figure 4. Figure 3 also contains the N-values predicted from the mean velocity using the geometric relation

$$N(x) = N_1(U(x)/U_1)^{1/2} \tag{3.1}$$

where the subscript 1 denotes conditions upstream of the contraction. The correspondence is excellent considering the experimental uncertainties. Relation (3.1) was therefore used whenever local values of N were needed.

The data described here were collected for two upstream stratification strengths: one weakly stratified having Brunt-Väisälä frequencies $N_1 = 0.62$ and $N_2 = 0.98$ rad s^{-1} and the other strongly stratified with $N_1 = 1.40$ and $N_2 = 2.22$ rad s^{-1}. Non-stratified runs were also performed for comparison.

3.3. *Instrumentation*

The velocity and temperature fluctuation measurements were made with an X-wire/cold-wire setup similar to that described in Lienhard & Van Atta (1990) consisting of a Dantec 55P61 X-wire 1.25 mm in length, with a cold wire sitting right next to it within 1 mm from the hot wires. The cold wire had a dual purpose: first of all it measured the fluctuating temperature and secondly its instantaneous measurements were necessary to correct the signals of the hot wires, which respond to instantaneous values of both the velocity and temperature of the flow. Extensive calibrations included variable yaw angle as well as variable velocity calibrations at different flow temperatures. The calibrations were performed before and after the experiments using a heated jet outside the tunnel.

The cold wires used were made inhouse as described in Thoroddsen & Van Atta (1993*b*). The wires were 0.75 mm long made of 0.65 μm diameter platinum wire, which gave sufficiently large length to diameter ratio to avoid attenuation due to prong effects.

Cross-stream integral length scales were estimated from two-point velocity mea-

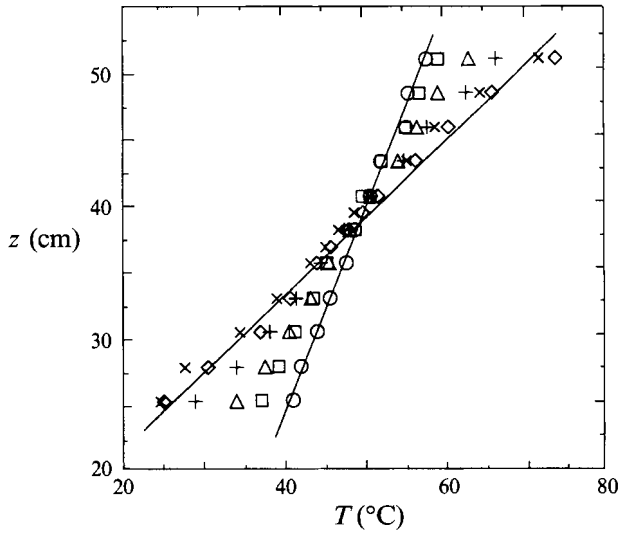

FIGURE 4. Mean vertical temperature profiles through the contraction, at streamwise locations relative to the contraction's entrance: ○, −14.0; □, 30.5; △, 43.2; +, 55.9; ◇, 81.3; ×, 106.7 cm. M = 2.54 cm, U_2 = 2.1 m s^{-1} and N_2 = 2.2 rad s^{-1}. The contraction extends 76.2 cm in the streamwise direction.

surements using two single hot wires spaced in the vertical direction. Similarly, cross-stream temperature scales were estimated from two-point temperature measurements using two cold wires. The separation of the two probes was varied using a micrometer and the initial separation was determined with a cathetometer to an accuracy of 0.05 mm, as described in Thoroddsen & Van Atta (1993*b*).

3.4. *Avoiding lee waves*

When designing the contraction one has to make sure that it does not generate lee waves in the test section, which would complicate the turbulence dynamics we wish to study here. The important parameter determining whether lee waves will be formed by the contraction is the global Froude number,

$$F = \frac{U}{NL} \tag{3.2}$$

where L is the vertical depth of the flow. For the strongest stratified case studied here this Froude number is $F_1 = 0.80$, where the subscript 1 stands for upstream and 2 for downstream of the contraction. The effect of the contraction is to increase the global Froude number, by $r^{3/2}$, where r is the contraction ratio which is 2.5 in our case. This gives $F_2 = 3.2$.

Following Scotti & Corcos (1972) (see also Turner 1973, p. 55 et seq.), we see that based on linear stability analysis lee waves will be formed only if $F \leqslant 1/\pi$. We can thus conclude that our flow is supercritical and the contraction will not generate lee waves for the experimental setup studied here.

The analysis above is of course limited to laminar flow and it is quite uncertain what will happen for a flow consisting of a combination of waves and turbulence. One might intuitively expect that the presence of turbulence would tend to reduce the formation of waves by its nonlinear energy transfer between the different components of velocity, relative to the case without turbulent transfer.

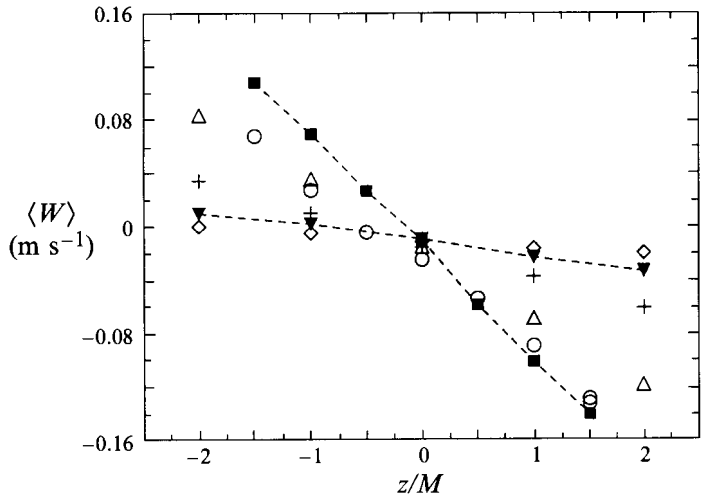

FIGURE 5. Changes in the mean vertical velocity at vertically off-centreline locations, for many streamwise locations inside the contraction.

3.5. *Vertical homogeneity of the turbulent field*

One does not expect the flow field to be homogeneous in the vertical direction owing to the vertical non-uniformity of the mean strain inside the contraction. To assess the magnitude and importance of these inhomogeneities we have performed systematic measurements off the centreline inside the contraction.

Figure 5 shows the changes in the mean vertical velocity as one moves off the centreline at many streamwise locations inside and near the contraction. The mean vertical velocity shows the expected change of sign as one traverses the centreline. The r.m.s. velocity fluctuations at the same locations are shown in figure 6 and are reasonably uniform.

The meaning of the vertical buoyancy flux is complicated off the centreline due to the non-zero mean vertical velocity component. Figure 7 shows the buoyancy flux, for $N_2 = 0.98$ rad s^{-1}, calculated by using its regular definition, i.e. by using the w-fluctuations about the mean, $\langle W \rangle$, at each vertical measurement location. The constancy of this quantity is remarkably good. Results for the stronger stratification are similar, as is included in particular for the buoyancy flux in figure 7. The main results presented in this paper, from measurements on the centreline, can thus be considered minimally affected by off-centre inhomogeneities through the contraction.

4. Results

Here we present the main results obtained from the different experimental configurations tested. For reference we will briefly review these configurations. Data were obtained for two stratification strengths, as well as for some *non-stratified* reference runs. The stronger stratification strength corresponded to $N_1 = 1.40$ rad s^{-1} entering the contraction and 2.22 rad s^{-1} leaving it, while the weaker one had, correspondingly, N of 0.62 and 0.98. Two different grid mesh sizes, $M = 2.54$ and 5.08 cm, were used to gauge the effects of varying the turbulent Reynolds number. Two different distances Δx from the grid to the entrance of the contraction were also used to study

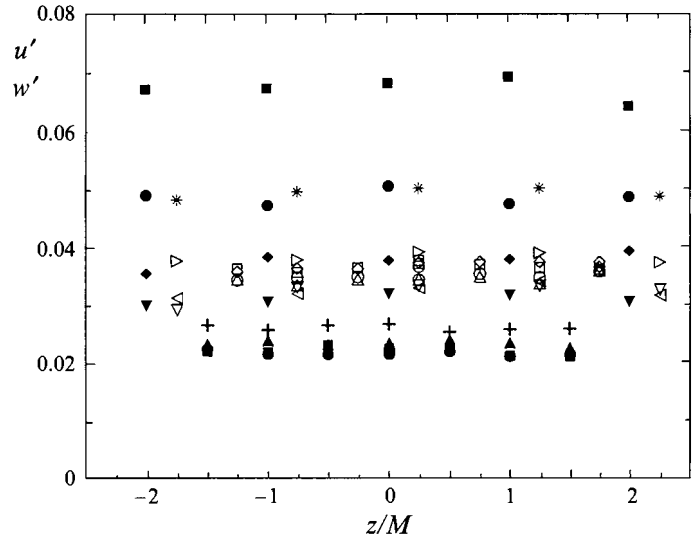

FIGURE 6. Vertical homogeneity of the r.m.s. velocity fluctuations, measured at numerous streamwise locations inside the contraction: w' (open symbols and *), u' (filled symbols and +). The z-axis for w' has been shifted by $M/4$ to avoid clutter of the various symbols. $M = 2.54$ cm.

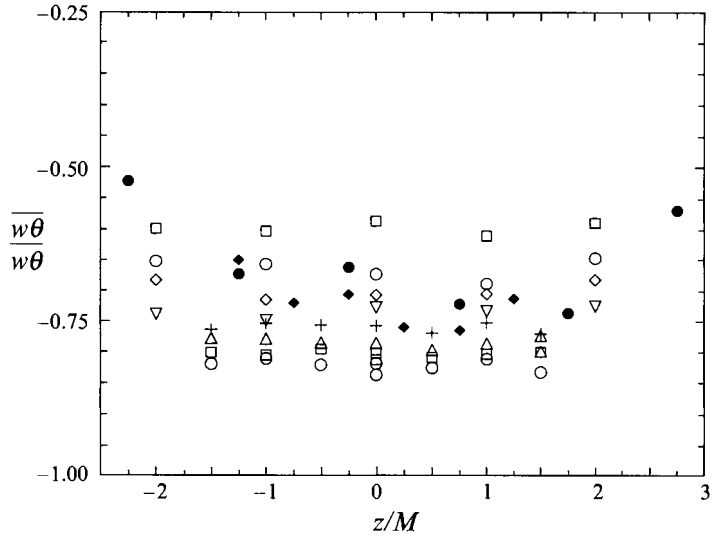

FIGURE 7. Vertical homogeneity of the buoyancy flux for $M = 2.54$ cm. Open symbols for $N_2 = 0.98$ rad s^{-1}. Filled symbols show results for $N_2 = 2.22$ rad s^{-1} and have been shifted $M/4$ in the z-direction to avoid clutter. The various symbols show different streamwise locations inside the contraction.

the effects of varying the importance of the 'initial' ratio of L_t/L_O as discussed in the introduction. These Δx were 48.3 and 101.6 cm. The dashed vertical lines in the figures mark the physical extent of the contraction. We will now describe and discuss the experimental results, focusing first on the r.m.s. quantities and the buoyancy flux and then on spectra and length scales of the turbulent motions. Tabular listings of the main results are available from the JFM Editorial Office.

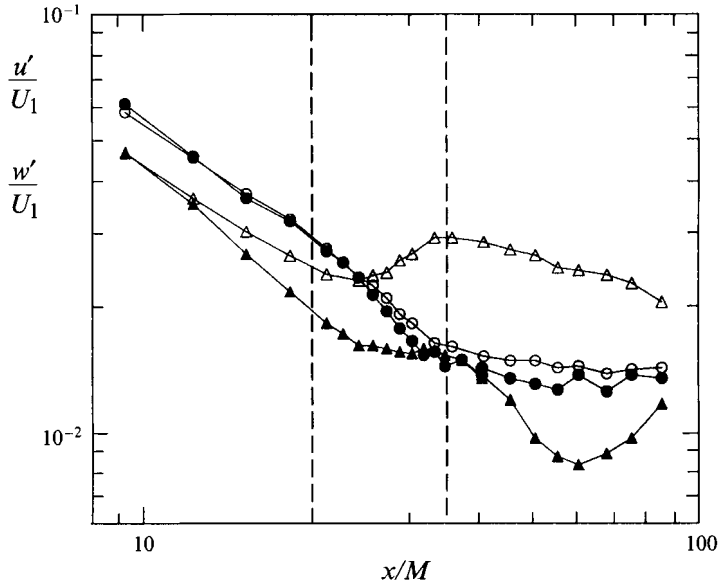

FIGURE 8. The effect of stratification on the r.m.s. velocities through the contraction, $M = 5.08$ cm: ○, u'; △, w'; open symbols show non-stratified results and closed symbols the stratified case, with $N_2 = 2.22$ rad s^{-1}. $\Delta x = 101.6$ cm.

4.1. *Velocity fluctuations*

The r.m.s. fluctuating velocities in the streamwise (u) and vertical (w) directions were measured all along the test section and through the contraction. Figure 8 shows the streamwise evolution of the velocity fluctuations for both stratified and non-stratified cases for $M = 5.08$ cm and $\Delta x = 102$ cm. The non-stratified evolution is in good agreement with that observed by Mills & Corrsin (1959) and Warhaft (1980), i.e. the vertical velocity fluctuations show the typical amplification due to vortex stretching. The streamwise component is little affected by the stratification, but the vertical one shows a dramatic qualitative difference due to the buoyancy. In the non-stratified case w' increases rapidly, dramatically overtaking u', while for the actively stratified case it barely catches up with u' and then suddenly collapses downstream of the contraction. Finally w' increases ('zombie' turbulence) through restratification farther downstream, as will be investigated in the following sections. The results for the smaller grid $M = 2.54$ cm are in good quantitative agreement with those described above for the larger grid. It should be pointed out that w' has already started diminishing relative to the u-component by the time the turbulence enters the contraction, owing to the well-known r.m.s.-anisotropy induced by the action of the relatively weak but significant buoyancy forces in the region between the grid and the entrance to the contraction (see for example Lin & Veenhuizen 1975 and Thoroddsen & Van Atta 1993*a*).

Figure 9 shows similarly the u' and w' for the shorter value of $\Delta x = 48.3$ cm. The behaviour of w' is intermediate between the unstratified and stratified case with $\Delta x = 102$ cm discussed above, as one might expect.

These observed effects can be qualitatively understood by a simple model in the spirit of Prandtl's homogeneous case analysis, keeping in mind Bjerknes theorem for

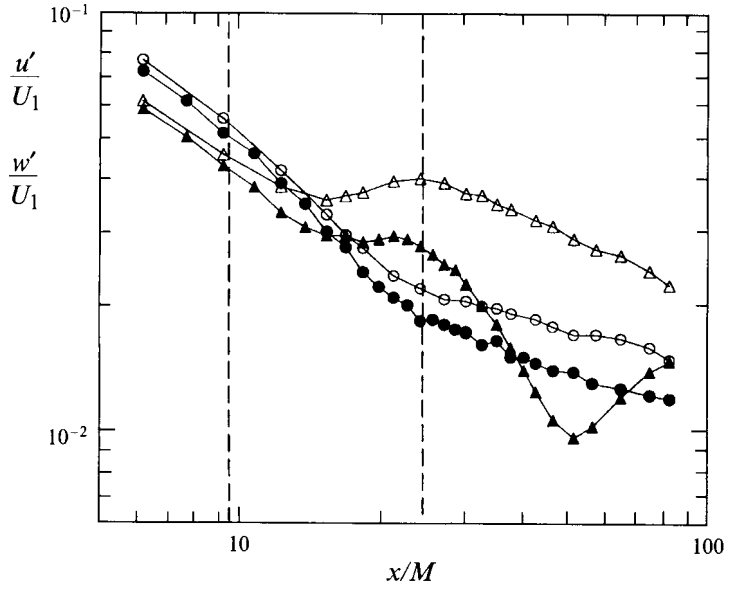

FIGURE 9. Same as in figure 8, but for $\Delta x = 48.3$ cm.

rate of change of circulation Γ around a path C bounding a surface S in a variable density fluid:

$$\frac{\mathrm{D}\Gamma}{\mathrm{D}t} = \int\int_S \frac{1}{\rho^2}(\nabla\rho \times \nabla p)\cdot \mathrm{d}\boldsymbol{A}. \tag{4.1}$$

A vortex with its axis in the stream direction will be weakened by baroclinic generation of vorticity as it displaces fluid vertically in the density gradient. The reduction in circulation of the vortex is accompanied by a reduction in the vertical velocity fluctuations relative to the unstratified case. This reduction is observed experimentally both preceding the contraction and inside it. A vortex with its axis in the vertical direction will be compressed. However, the vortex flow field is horizontal and no new effects, due to buouyancy on the velocity fluctuations, will be produced. A vortex with its axis in the cross-stream direction will not be stretched by our two-dimensional contraction, but will be weakened by baroclinic generation, contributing to some decrease in the vertical and horizontal velocity fluctuations, as observed.

The strong rebounding of w', in the region farthest downstream, cannot be explained by the tendency of anisotropic velocity fields to return toward isotropy. This is clear from the cross-over of the u' and w' components shortly after the flow leaves the contraction, which should be contrasted with the very slow return to isotropy after the contraction for the non-stratified data shown in the same figure. The slow return to isotropy, of the velocity field, was also found by Warhaft (1980, figure 2) for the passive-scalar non-stratified case.

4.2. *The velocity spectral shapes formed by the mean strain*

We compare now the vertical velocity spectra for the stratified and non-stratified experiments discussed above, to pinpoint the length scales associated with the buoyancy effects. The spectral relations of isotropic turbulence do not hold for turbulence under external strain as experienced inside the contraction, but we use these relations here as a convenient qualitative tool to investigate the selective amplification of the

vertical velocity spectrum relative to the streamwise spectrum, to determine for which length scales the energy is most amplified by the stretching.

The isotropic spectral relations between the two one-dimensional spectral components are (Hinze 1975, p. 204)

$$E_{ww}(k_1) = \frac{1}{2}\left(E_{uu}(k_1) - k_1 \frac{\mathrm{d}E_{uu}(k_1)}{\mathrm{d}k_1}\right).$$

We use this relation only to predict $E_{ww}(k_1)$ from the measurements of the $E_{uu}(k_1)$-spectrum and do not expect it to be satisfied in the spectral plots shown here, not even for the non-stratified cases, owing to the drastic affects of the mean strain. We call this predicted w-spectrum $E^P_{ww}(k_1)$. We then compare the measured $E_{ww}(k_1)$ to $E^P_{ww}(k_1)$ and investigate which length scales deviate most from the prediction. Figure 10(*a*) shows the amplification of $E_{ww}(k_1)$ for the non-stratified case, shortly after the contraction's end, at $(x/M = 5)$. The energy of the largest scales is amplified while that of the small scales remains virtually unchanged or is even slightly attenuated. Figure 10(*b*) shows the corresponding spectra for the stratified case. The large-scale amplification of the vertical velocity is significantly reduced by the buoyancy. The separation wavenumber ($k \approx 125$ rad m^{-1}), marking the smallest scales amplified, remains about the same, while the large-scale amplification level reduces by about a factor of 3. Note that the spectral predictions in figures 10(*a*) and 10(*b*) are different since the u-spectra are different for these two cases.

The changes in $E_{ww}(k_1)$ farther downstream will be investigated in a later section.

4.3. *Buoyancy flux*

The vertical buoyancy flux $-\overline{w\theta}/(w\theta)$ was measured along the entire length of the flow field including through the contraction. Figure 11 shows the results for the shorter Δx (= 48.3 cm) and figure 12 for the longer Δx (= 101.6 cm).

For the smaller Δx the flux has not begun any substantial collapse due to buoyancy forces at the entrance to the contraction. Only a slight initial reduction is noticed for the smaller mesh sized grid. The contraction enhances the flux which, in the absence of the contraction, would decay monotonically after an initially constant flux. The flux evolution after the contraction's exit is similar to what would be expected if the turbulence was generated by a grid located at its exit, with two important exceptions, i.e. the relative quickness with which it collapses and the very large negative values for the countergradient fluxes produced in the restratification region. This may be due to the strength of the fossilization of the density field, which quickly damps the vertical turbulent velocities, and buoyancy overpowering the nonlinear transport. The x-location where the flux reverses sign coincides with the minimum in the r.m.s. vertical velocity shown in figure 8 and the maximum in θ shown in figure 16. This clearly demonstrates the conversion of vertical kinetic energy into potential energy. This potential energy is then returned from the density field back into the vertical velocity component as the fluid elements begin to drift back to their equilibrium locations in the mean density field, as is further discussed in §4.5. The flux falls off faster for the smaller grid, consistent with Froude number scaling. It also collapses slightly sooner after leaving the contraction. The restratification is much stronger than that measured in decaying grid generated tubulence without a contraction. The weaker stratification (included in figure 11) shows continuing stirring and down-gradient flux downstream of the contraction.

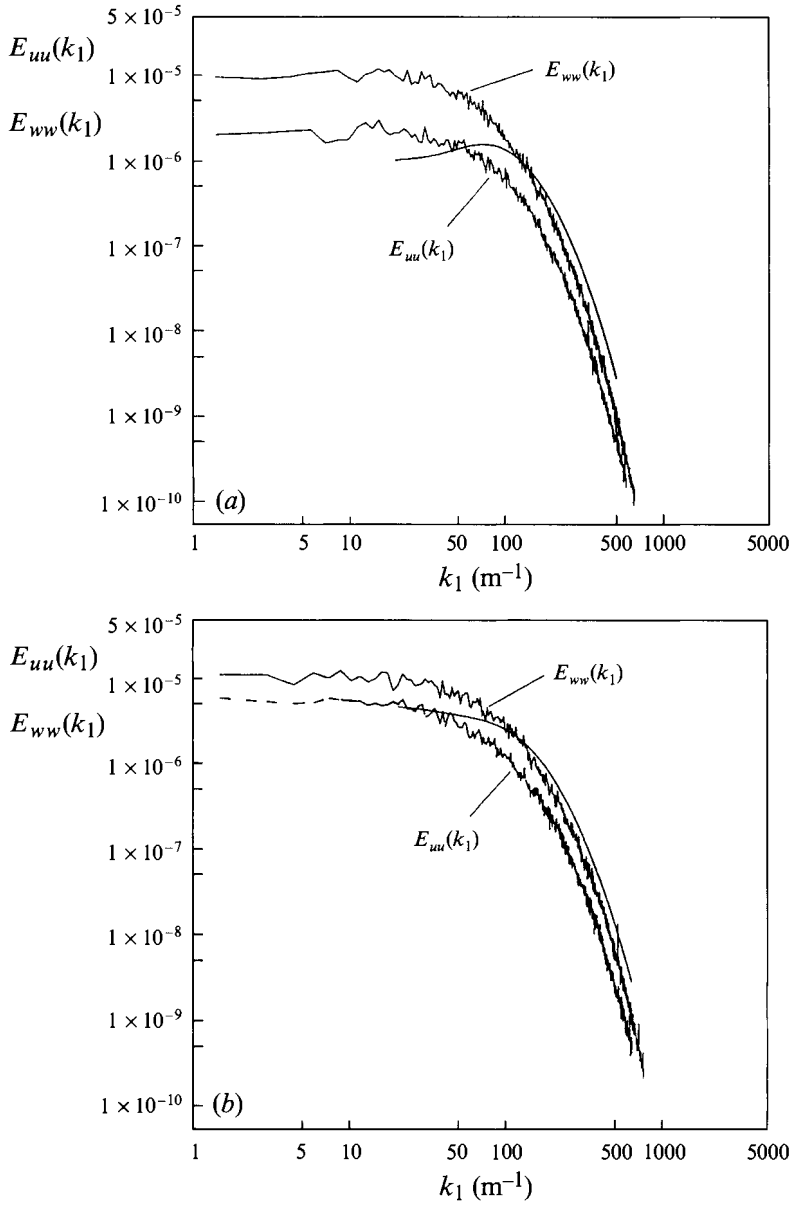

FIGURE 10. Comparison of the measured vertical velocity spectrum with the spectrum predicted from the streamwise velocity using the isotropic relations (smooth line), at $x/M = 5$ downstream of the end of the contraction, $\Delta x = 101.6$ cm, $M = 5.08$ cm: (*a*) non-stratified, (*b*) stratified run.

The data farthest downstream in figure 11 were collected at a much later date than the rest of the study and show the flux for a slightly higher N_2 ($= 2.37$ rad s^{-1}), as is evident by the counter-gradient flux occurring earlier, resulting in some mismatch in the curves.

The rate at which the normalized buoyancy flux $-\overline{w\theta}/(w'\theta')$ reduces is much quicker in these experiments than in the decaying grid turbulence without the contraction.

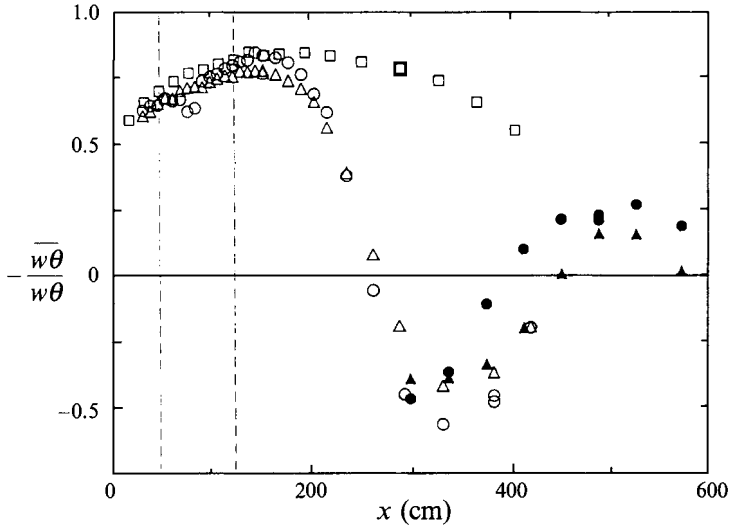

FIGURE 11. Normalized buoyancy flux through and after the contraction *vs.* distance from the grid for $\Delta x = 48.3$ cm. $N_2 = 2.22$: ○, $M = 2.54$ cm and △, $M = 5.08$ cm. $N_2 = 2.39$: •, $M = 2.54$ and ▲, $M = 5.08$ cm. For the weaker stratification $N_2 = 0.98$: □, $M = 5.08$ cm.

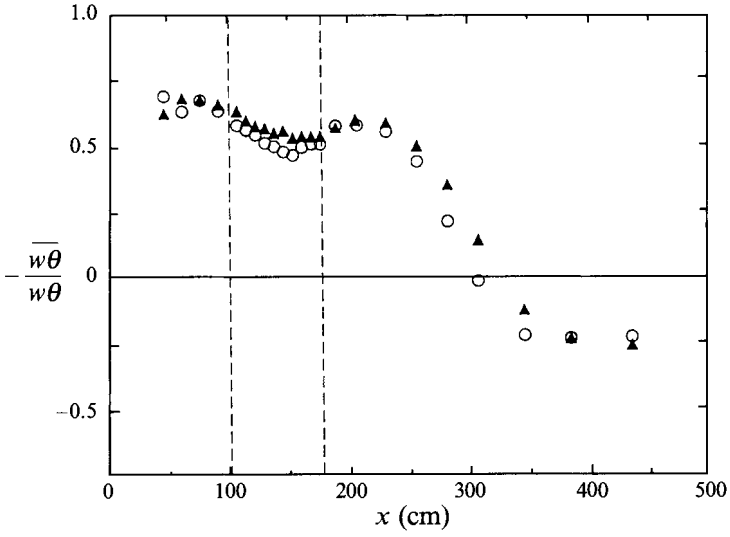

FIGURE 12. Normalized buoyancy flux *vs.* distance from the grid, for $\Delta x = 101.6$ cm and $N_2 = 2.22$: ○, $M = 2.54$ cm and ▲, $M = 5.08$ cm.

This rate can be normalized for comparison with other experiments in the following manner:

$$\text{rate} = \frac{-\Delta[\overline{w\theta}/(w'\theta')]}{N\Delta t}$$

where Δt is the time over which the change in the normalized flux is estimated, i.e. $\Delta x/U$. The results are listed in table 1 and show that the rates observed here are up to three times faster than for the decaying stratified turbulence without a contraction.

M (cm)	$\Delta x = 48.3$ cm	$\Delta x = 101.6$ cm	No contraction
2.54	1.3	0.81	0.50
5.08	1.1	0.69	0.35

TABLE 1. The rate of buoyancy flux collapse

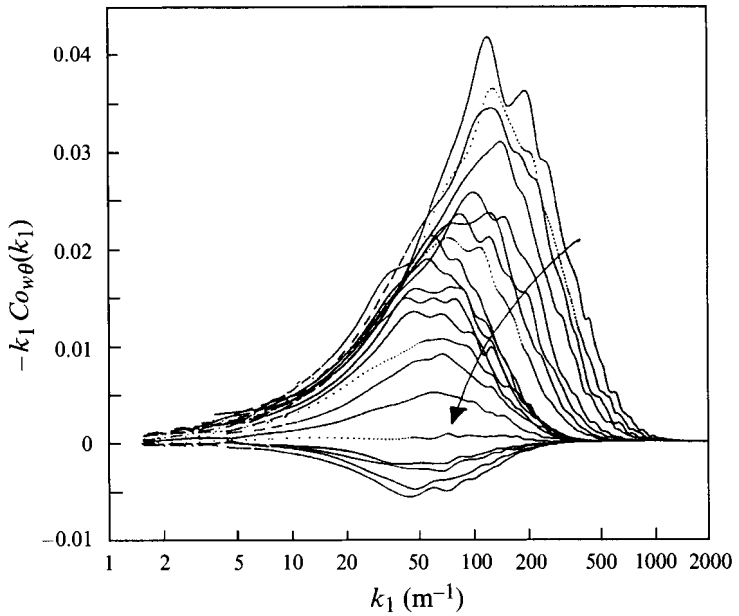

FIGURE 13. Cospectra of vertical velocity and temperature *vs.* downstream location, for $\Delta x = 101.6$ cm, $M = 5.08$ cm. The arrow shows the evolution from the grid downstream.

The very similar quantitative behaviour of the buoyancy flux measured using the two different grid sizes, indicates that Re_λ is large enough to allow us to study the interactions of buoyancy and inertia, not directly affected much by viscous forces.

4.4. *Cospectra between w and θ*

The length-scale composition of the buoyancy flux was studied by looking at the cospectra of w and θ. Figure 13 shows the monotonic decrease in $Co_{w\theta}$ with increasing x. These results demonstrate that all scales restratify indicating total extinction of the turbulent cascade transfer of energy and the associated mixing. It has been clearly demonstrated in the non-contracted experiments of Lienhard & Van Atta (1990) that restratification starts at the large scales and can coexist with down-gradient flux at the small scales. In the current experiments this is contrasted by restratification at all active scales of motion, due to the very sudden increase in N.

Measurements further downstream (not presented here) show another cycle of positive and negative cospectra. It should be pointed out that the meaning of the cospectra for the random field of bobbing fluid volumes is obscured from the regular interpretation applied to actively turbulent stirring and mixing. The change in sign of $Co_{w\theta}$ does not necessarily mean re-emergence of nonlinear turbulent transfer, but rather may only signify that the bobbing fluid volumes have overshot their equilibrium locations.

4.5. *Vertical velocity spectra in the restratification region*

Figure 14 shows the spectra of vertical velocity leading up to and inside the restratification regime. In figure 14(*a*) the vertical velocity spectrum decays monotonically at all scales due both to buoyancy at large scales and viscous dissipation at small scales. Then farther downstream the vertical velocity revives again as was shown by the w' results in figure 8. Figure 14(*b*) shows that the scales initially receiving the energy from the nearly fossil potential energy are very large scales, i.e. > 40 cm. Then, as is shown in the last two measured spectra, at N_2x/U_2 between 4.3 and 4.8 rad (x from 3.1 to 4.3 m), this energy is being transferred to smaller scales. Similar measurements were carried out farther downstream in a later set of experiments, beyond the data shown in figure 9. These measurements, shown in figure 15, reveal a *second cycle* of 'zombie' revival, now occurring at somewhat larger wavenumbers. Results for $M =$ 5.08 cm (not shown here) show an identical trend.

The scale at which the restratification initially revives $E_{ww}(k_1)$ is larger than the integral scales of the temperature field, but one should also keep in mind the aliasing of the one-dimensional spectra with respect to the three-dimensional spectrum which makes the scales based on the one-dimensional spectra appear larger, as discussed for a similar situation in Thoroddsen & Van Atta (1993*a*).

4.6. *Temperature fluctuations*

The level of fluctuating temperature depends on local quantities, such as the size of the turbulent overturns and the local mean temperature gradient, as well as on the scalar dissipation rates. However, when the turbulent structure is not in a 'local equilibrium', the fluctuation level will also depend on the previous history of the flow, such as the level of large-scale fossilization of the scalar field by the buoyancy. Figure 16 shows the temperature fluctuations for both Δx and both mesh sizes. The fluctuations grow continuously through the contraction, but then decay farther downstream. Measurements 4 cm vertically off-centre (not shown here) show very similar results. To account for the effects of the increase in the mean temperature gradient we next normalized the temperature fluctuations by $\mathrm{d}T/\mathrm{d}z(x)$, which by definition gives us L_t. This scale is shown in figure 17. The clear difference in L_t between the two different Δx cases shown in this figure again demonstrate the effects of the different strength of buoyancy. The larger Δx case shows a very sharp drop in L_t, due to the reduced overturning ability of the large scales. Figure 17(*a*) includes the results from the weaker stratification and the comparison clearly demonstrates the continual growth in L_t when the inhibitive effects of buoyancy forces are not present.

The increase of θ' through the contraction can also be understood by a simple extension of Prandtl's circular vortex model. Assume that θ' produced by a vortex is given by the product of the mean temperature gradient and the vertical length scale (D = diameter) of the vortex:

$$\theta' = \frac{\mathrm{d}T}{\mathrm{d}z} D. \tag{4.2}$$

For a streamwise vortex, continuity gives $D_2/D_1 = 1/r^{1/2}$ where D_2 and D_1 are the vortex diameters downstream and upstream of the contraction, respectively. The mean temperature gradient increases at the same time by r. From (4.2) with $r = 2.5$ we therefore have $\theta'_2/\theta'_1 = 1.6$. Vertically oriented vortices produce no temperature fluctuations in this model and hence no effect on θ'. Lateral vortices would be flattened by a factor of $1/r$ and (4.2) predicts no effect on θ'. For the data in figure

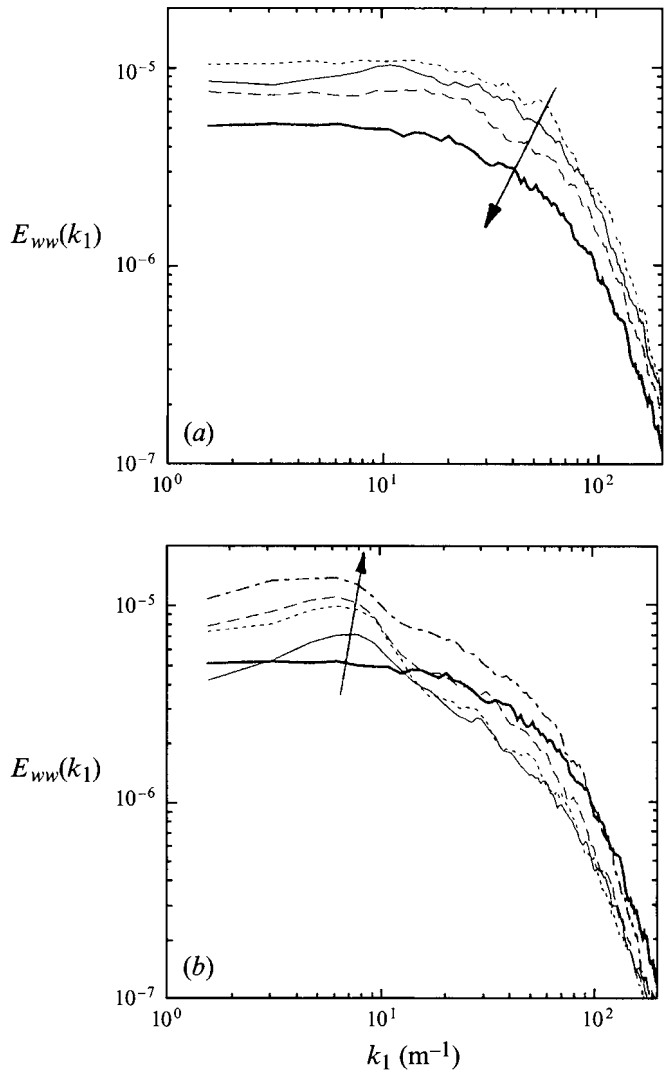

FIGURE 14. Vertical velocity spectra approaching and inside the restratification region, showing how the large scales gain vigour through the restratification. (*a*) The vertical velocity spectra decay monotonically. (*b*) Restratification revives the vertical velocity fluctuations, first at the large scales. Then further downstream the small scales also show increased energy due to spectral transfer. Spectra are shown for N_2x/U_2 = 3.4 (—), 3.8 (· · ·), 4.3 (– – –) and 4.8 (–· –) rad, corresponding to x between 3.1 and 4.3 m. Δx = 101.6 cm and M = 5.08 cm. The spectrum denoted by the bold line is identical in both (*a*) and (*b*) to facilitate the comparison.

16, θ_2'/θ_1' ranges from 1.2 to 2.0, bracketing the prediction of the model. This model contains no reference to variable density effects and should be considered as a passive scalar limit.

4.7. *Temperature spectra*

We show here the downstream evolution of the temperature spectra for three different cases, i.e. the weak stratification and the two more strongly stratified cases. We first compare the two stratifications for the shorter Δx. Figure 18 shows the one-

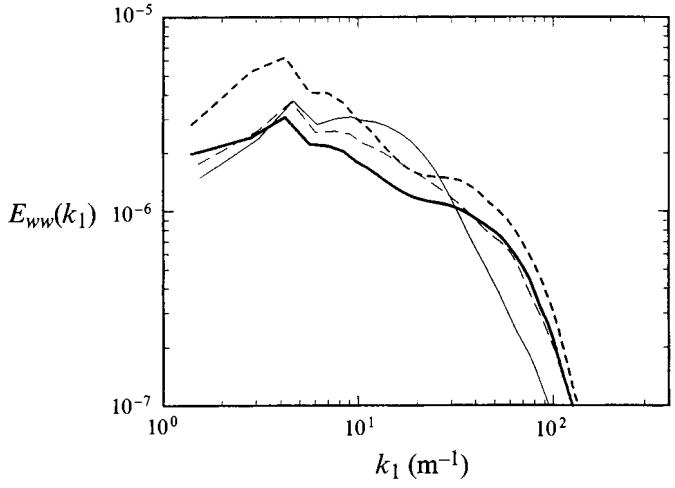

FIGURE 15. Vertical velocity spectra from separate measurements farthest downstream in the test section, showing a second cycle of zombie revival, for $N_2 = 2.37$ rad s^{-1} and $\Delta x = 48.3$ cm. $M = 2.54$ cm; $N_2x/U_2 = 3.36$ (——); 4.22 (– – –); 5.51 (- - -); 6.46 (—), corresponding to x/M between 117 and 225.

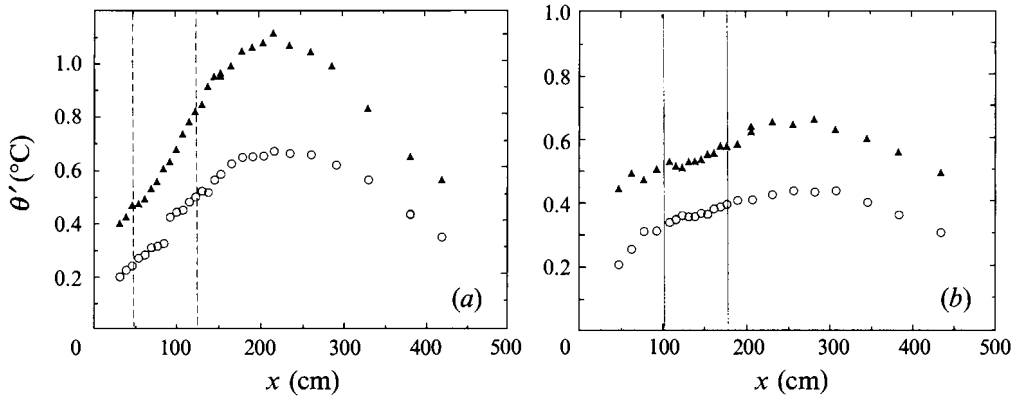

FIGURE 16. Temperature fluctuations, θ_{rms}, in °C, *vs.* downstream location, for $M = 5.08$ cm (solid triangles) and 2.54 cm (open circles): (*a*) $\Delta x = 48.3$ cm, (*b*) $\Delta x = 101.6$ cm.

dimensional temperature spectra at numerous streamwise locations for $M = 5.08$ cm and $N_2 = 2.22$ rad s^{-1}. Figure 18(*a*) shows $E_{\theta\theta}(k_1)$ upstream and inside the contraction. Initially the small-scale fluctuations decay monotonically and the energy at the large scales grows strongly due to the vortex stretching, similar to $E_{ww}(k_1)$ shown in §4.2. The spectra appear to pivot around a fixed length scale. Farther downstream the temperature spectral shape reaches a nearly steady form starting at the exit of the contraction. Figure 18(*b*) shows that the spectra from N_2x/U_2 between 1.29 and 4.43 rad (x from 1.2 to 4.2 m) possess very similar shapes and only the last three spectra show any significant reduction in fluctuation levels. This signifies a balance between generation of temperature fluctuations by the flux and destruction by molecular dissipation, or may imply fossilization, i.e. the shut-off of the turbulent stirring process at the large scales. Figure 19 shows the corresponding evolution of $E_{\theta\theta}(k_1)$ for the weaker stratification. The response of the spectral shape to the strain

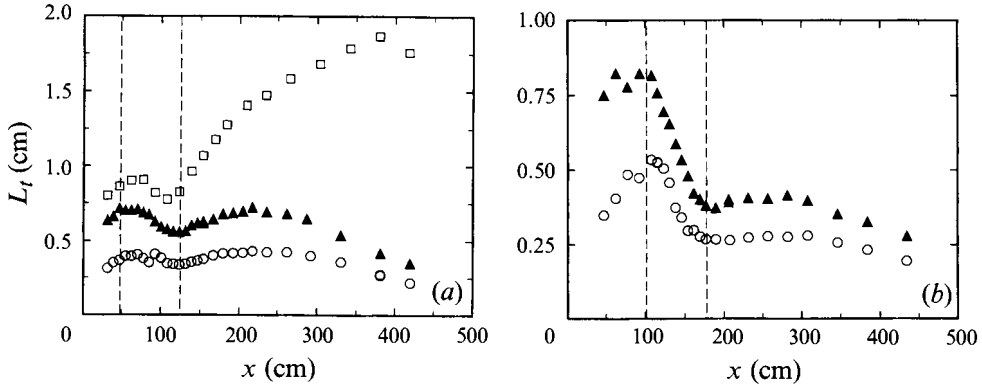

FIGURE 17. Overturning scale, L_t *vs.* downstream location, for $N_2 = 2.22$ rad s^{-1} and $M = 2.54$ cm (open circles) and $M = 5.08$ cm (solid triangles): (*a*) $\Delta x = 48.3$ cm, (*b*) $\Delta x = 101.6$ cm, Open squares show data for $N_2 = 0.98$ rad s^{-1}.

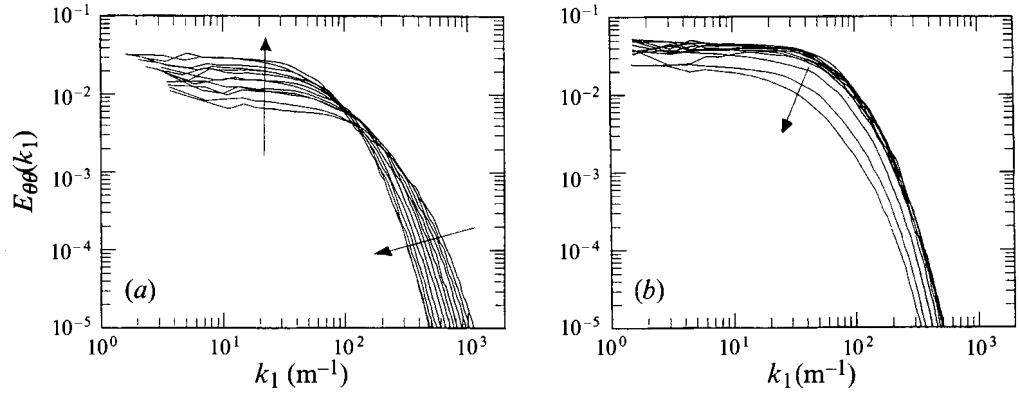

FIGURE 18. Evolution of the temperature spectrum downstream from the grid, for $N_2 = 2.22$ rad s^{-1} and $\Delta x = 48.3$ cm. (*a*) Upstream and inside the contraction for N_2x/U_2 from 0.33 to 1.34 (x = 30.5 – 124 cm). The high-wavenumber energy decays monotonically in the beginning, but then the spectra start collecting onto one curve at $x \approx 125$ cm. (*b*) Spectra downstream of the contraction, for N_2x/U_2 from 1.34 to 4.54 rad (x = 122 – 419 cm).

is similar, but downstream of the contraction the spectra keep growing (figure 19(*b*)), clearly showing the difference due to the influence of buoyancy. The near-passive stratification allows the turbulence to continue to transport in fluid parcels from farther away in the background mean gradient.

Figure 20 shows the data for the larger $\Delta x = 101.6$ cm and these spectra should be compared to those in figure 18. The strain inside the contraction does not manage to amplify the large scales to any significant extent as is implied by the sharp decline in L_t in figure 17. The spectral shape again becomes approximately invariant for some distance downstream of the contraction.

4.8. *The vertical energy balance*

The vertical energy balance in the flow is governed by the exchange of energy between kinetic energy and the potential reservoir, as discussed in §2. The vertical kinetic $\overline{T_w}$ and potential $\overline{\Psi}$ energies are shown in figures 21(*a*) and 21(*b*) for the three different

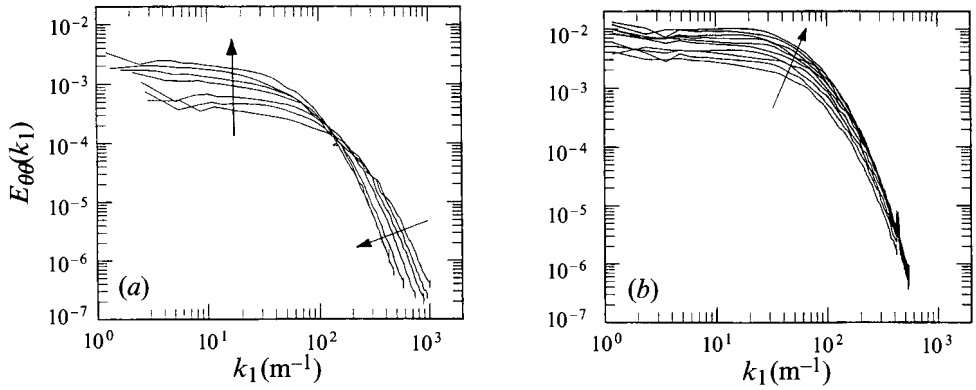

FIGURE 19. Same as figure 18, for the weakest stratification $N_2 = 0.98$ rad s^{-1}, $M = 5.08$ cm and $\Delta x = 48.3$ cm. (*a*) Upstream and inside the contraction. (*b*) Downstream of the contraction.

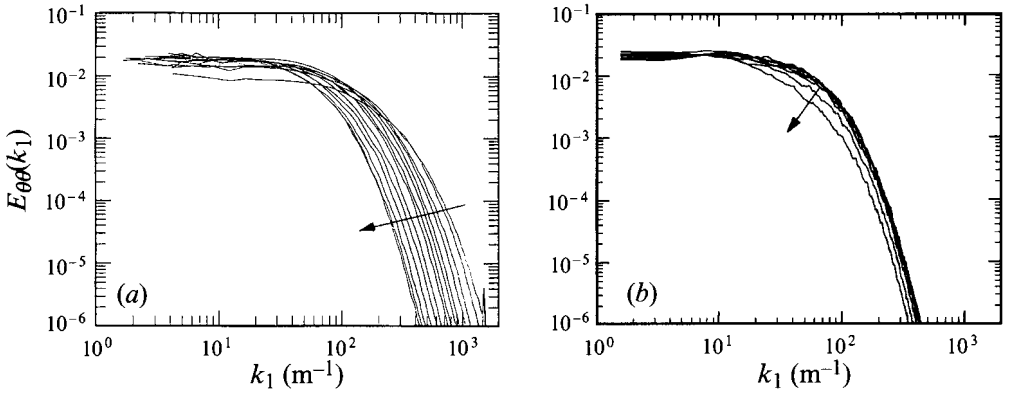

FIGURE 20. Same as figures 18 and 19, for $\Delta x = 101.6$ cm for the most strongly stratified case. (*a*) Upstream and inside the contraction. (*b*) Downstream of the contraction.

cases discussed in the previous subsection. The decay in vertical kinetic energy is delayed in all of the cases as the turbulence is strained by the contraction as expected. The potential energy, on the other hand, shows significant differences depending on Δx, i.e. the ratio L_t/L_b. For the larger Δx the growth in $\overline{\Psi}$ is reversed inside the contraction as buoyancy quells the overturning eddies. Downstream of the contraction $\overline{T_w}$ and $\overline{\Psi}$ oscillate around a common mean. At the point of minimal vertical kinetic energy, the value of $\overline{T_w}$ is only about 30% of that of $\overline{\Psi}$.

Significantly these results show $\overline{\Psi}$ become larger than $\overline{T}$. For decaying grid turbulence in thermally stratified air, Lienhard & Van Atta (1990) did not see $\Psi > T$, whereas Itsweire *et al.* (1986) did find this for a higher Schmidt number in salt-stratified water.

4.9. *Integral length scales of velocity*

To gain further insight into the evolution of the spatial length scales as the turbulence passes through the contraction we conducted some separate two-point correlation measurements. The streamwise velocity component was measured at two spatial points separated in the vertical direction, using two single hot wires, mounted on a micrometer stage. This allowed for accurate adjustments of the Δz separation

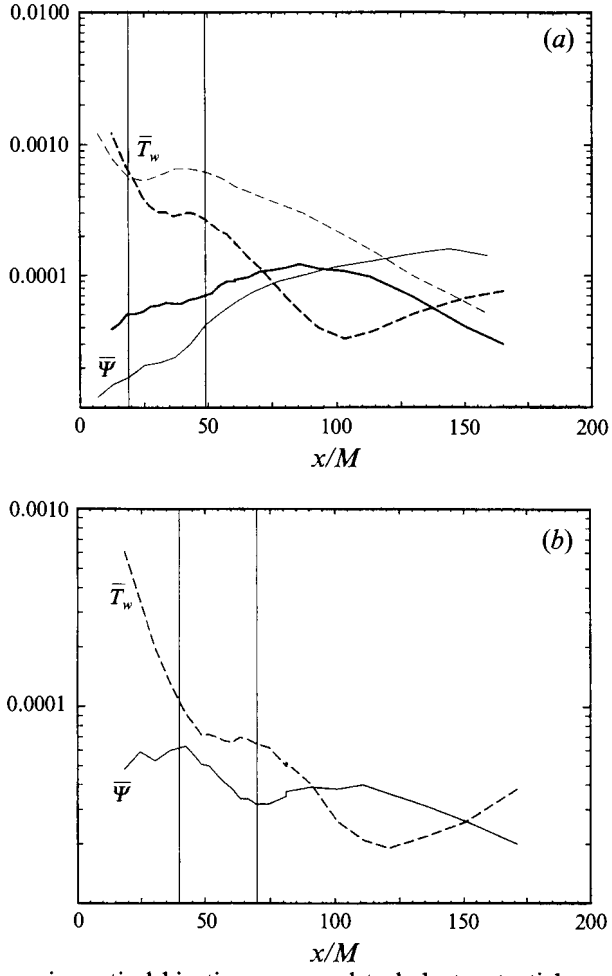

FIGURE 21. Changes in vertical kinetic energy and turbulent potential energy through and downstream of the contraction for $M = 5.08$ cm. (*a*) $\Delta x = 48.3$ cm: thicker lines for the stronger stratification and narrower lines show results for the weaker stratification, (*b*) $\Delta x = 101.6$ cm, for the stronger stratification only.

of the two wires. From these measurements the longitudinal and vertical integral length scales were evaluated, to complement our previous discussion of Warhaft's (1980) length-scale spectral data. We studied, in this way, only the non-stratified flow through the contraction. The complication of the temperature corrections of the hot wires for the stratified case would have made those two-point measurements exceedingly difficult. This part of the study was conducted at a somewhat larger mean velocity ($U_2 \approx 3$ m s^{-1}) than the facility allowed for the stratified runs ($U_2 \approx 2.1$ m s^{-1}). Figure 22 shows the changes in the spectral peaks for $E_{uu}(k_1)$ and $E_{ww}(k_1)$, obtained with an X-wire, as the flow passes through the contraction. The location of the peak in the streamwise spectra stays unchanged, whereas the peak in the vertical spectra moves to smaller wavenumbers by approximately the contraction ratio. This agrees exactly with the results of Warhaft discussed in §2.

The spatial correlation, $R_{uu}(\Delta z)$, was studied only for the shorter $\Delta x = 48.3$ cm. Some of these correlation curves as well as those for $R_{uu}(\Delta x)$ are shown in figure 23. The delay in growth of the integral scales inside the contraction is clear from the

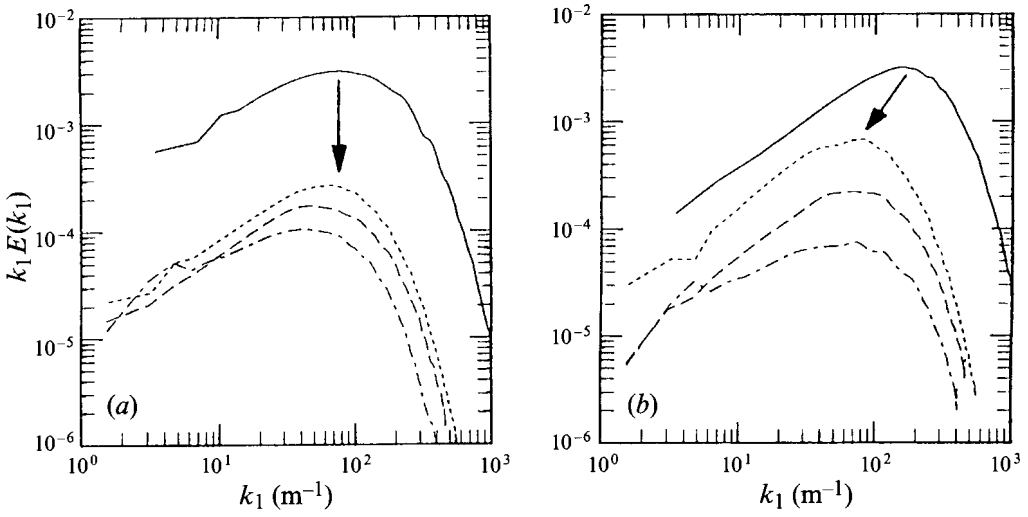

FIGURE 22. The changes in velocity spectral peaks as the flow passes through the contraction. (*a*) Longitudinal velocity spectra, (*b*) vertical velocity spectra.

small observed changes in these curves. We integrated the correlation curves to obtain the integral scales. Since in our measurements we did not attain sufficiently wide separation distances in the transverse z-direction to pinpoint the zero-crossing of $R_{uu}(\Delta z)$ we have here used a qualitative approach, by integrating the R-curves only up to the separation where the correlation falls to a small but positive value R_α, i.e.

$$\Lambda_i = \int_0^\beta R_{uu}(\Delta x_i)\, \mathrm{d}\Delta x_i \tag{4.3}$$

where

$$R_{uu}(\beta) = R_\alpha$$

and no summation is implied.

Figure 24 shows the ratios of Λ_z and Λ_x for R_α between 0.1 and 0.3. All of the curves portray the same trend. There is only a very slight *reduction* in Λ_z relative to Λ_x through the contraction, showing that the velocity field has some time to adjust to the mean strain. There is a large difference between the actual values of these two integral-type length scales Λ_x and Λ_z, as explained below, but what is important in this context are the relatively small changes in the ratio, as the flow experiences the strain through the contraction.

It should be pointed out that the difference in the definitions of Λ_x and Λ_z, i.e. the former is a longitudinal correlation and the latter a transverse correlation, will lead to different correlation shapes for $R_{uu}(\Delta x)$ and $R_{uu}(\Delta z)$, even in the isotropic case. The integrals of the two correlations will therefore be different. Using the isotropic relation and the measured $R_{uu}(\Delta x)$-curve we can numerically integrate and calculate the ratio Λ_z/Λ_x as a function of R_α. Noting the isotropic relations for the transverse correlation $g(r)$ in terms of the longitudinal correlation $f(r)$, Hinze (1975) or Taylor (1935),

$$g(r) = f(r) + \frac{r}{2}\frac{\mathrm{d}f(r)}{\mathrm{d}r}, \tag{4.4}$$

it is straightforward to estimate the ratio of the two length scales defined by (4.3) for

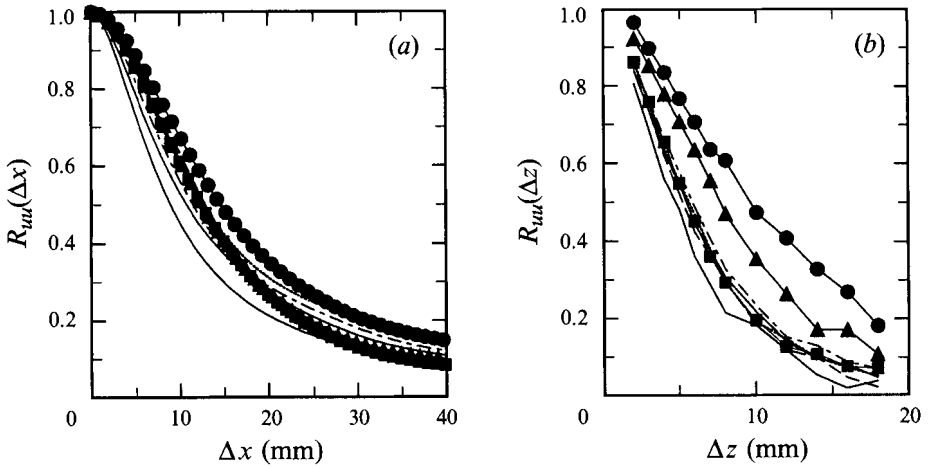

FIGURE 23. Streamwise auto- and cross-correlations of velocity through the contraction, which extends from $x = 48$ cm to 125 cm from the grid. The different curves are for different distances from the grid. $M = 2.54$ cm (*a*) Autocorrelations, (*b*) transverse cross-correlations for the same streamwise locations as in (*a*). The same curve symbols in (*a*) and (*b*) correspond to the same x location.

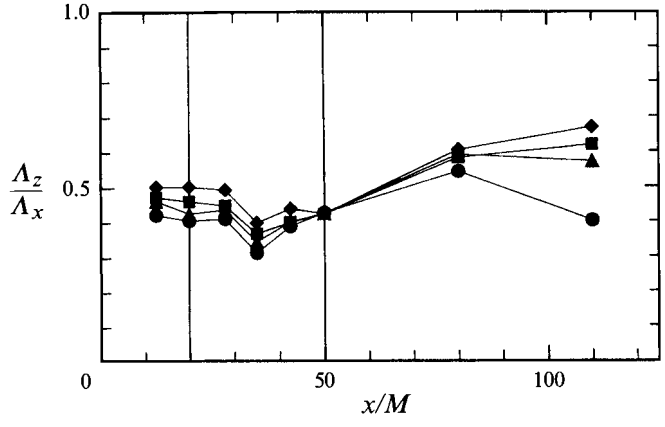

FIGURE 24. Ratio of the integral scales in z and x calculated from (4.3), for $R_\alpha = 0.10$ (•); 0.15 (▲); 0.20 (■); 0.30 (◆).

any R_α-level by numerically integrating the following equation using the measured $f(r)$:

$$\frac{\Lambda_z}{\Lambda_x} = 1 + \frac{1}{2}\frac{\int_0^\beta rf'(r)\mathrm{d}r}{\int_0^\beta f(r)\mathrm{d}r}. \tag{4.5}$$

This shows that, since $f'(r)$ is negative in the range studied, the ratio above is smaller than 1. This integration was performed using the measured $R_{uu}(\Delta x)$ (e.g. $f(r)$) and yielded values for this ratio in the range $0.4 - 0.6$, consistent with the measurements shown in figure 24.

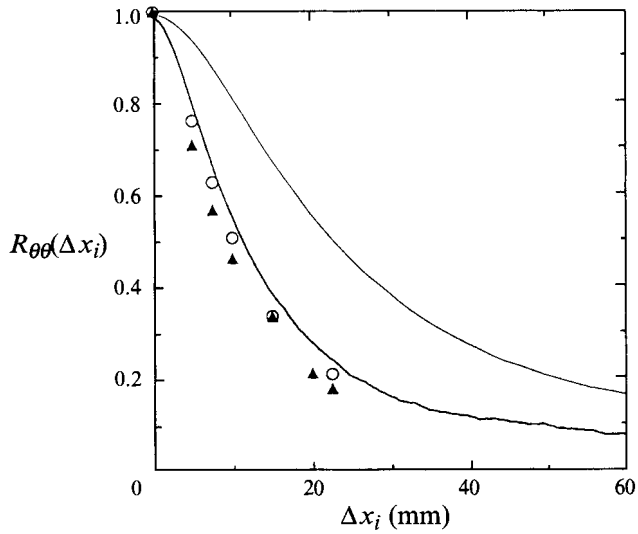

FIGURE 25. Spatial correlations of temperature in the streamwise and vertical directions for Δx = 48 cm, M = 5.08 cm and N_2 = 0.98 rad s^{-1}. $R_{\theta\theta}(\Delta x)$: ——, x = 50.8 cm: —, x = 88.9. $R_{\theta\theta}(\Delta z)$: ▲, x = 50.8 cm; ○, x = 88.9.

4.10. *Integral scales of temperature in x and z through the contraction*

The structure of the temperature field in both the vertical and streamwise directions is important for characterizing the dynamics of the density field as active, fossil or zombie turbulence. The squeezing of the temperature field through the contraction was investigated by measuring the spatial correlations of temperature both in the vertical direction, using two cold wires, and in the streamwise direction by applying Taylor's hypothesis. Figure 25 shows a typical set of temperature correlations for separations in both the x- and z-directions.

Since the separation of the two cold wires in the z-direction was not sufficiently large to allow for the integration of the correlation curves to the zero-crossing we used the 0.5 correlation contour to determine the length scales Θ_z and Θ_x, i.e. the separation length where the correlation has fallen to 0.5:

$$R_{\theta\theta}(\Delta x = \Theta_x) = R_{\theta\theta}(\Delta z = \Theta_z) = 0.5.$$

This was done for both the strong and weak stratifications. The resulting ratio of Θ_z and Θ_x is shown in figure 26 for both stratification strengths. These results show clearly that the spatial large-scale structure of the scalar field develops similarly inside the contracting zone irrespective of stratification strength for this Δx = 48.3 cm. Through the contraction the streamwise length scale grows drastically while the vertical one remains about the same. The straining inside the contracting zone can be used to predict this from the area ratio at each streamwise location. The curves for both r^{-1} and r^{-2} have been included in figure 26. The ratio appears to behave more like r^{-1} than r^{-2}, where r is the local contraction ratio.

The results for the near passive case, combined with those in the previous subsection, indicate that the large-scale temperature field is governed by the straining, whereas the velocity integral scales are much less affected by the mean strain.

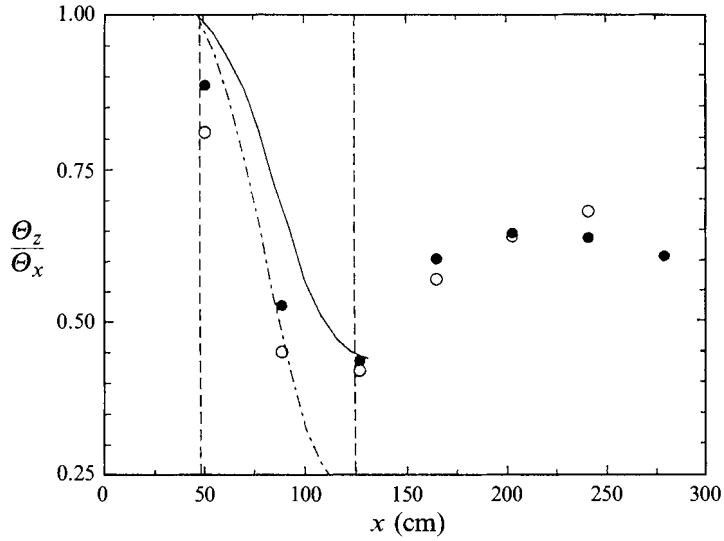

FIGURE 26. The ratio of the thermal integral length scales in z and x defined in §4.10, for $\Delta x = 48.3$ cm and $M = 5.08$ cm: ○, $N_2 = 0.98$ and •, $N_2 = 2.22$ rad s^{-1}. The vertical lines mark the extent of the contraction, whereas the curved lines shows functions of the local contraction ratio: – - –, r^{-2} and —, r^{-1}.

4.11. *Energy and scalar dissipation rates, ϵ and χ*

Figure 27 shows the energy dissipation rates which were calculated by integrating the velocity gradient spectra, $k_1^2 E_{uu}(k_1)$ and $k_1^2 E_{ww}(k_1)$, up to the wavenumbers where the spectra descend to the noise level at each streamwise location. The two velocity gradient variances were then combined using Stillinger's formula to estimate ϵ, i.e.

$$\epsilon = \nu \left[10 \overline{\left(\frac{\partial u}{\partial x}\right)^2} + \frac{5}{2} \overline{\left(\frac{\partial w}{\partial x}\right)^2} \right]. \tag{4.6}$$

The accuracy of this formula is unclear for small turbulent Froude numbers, as discussed by Thoroddsen & Van Atta (1992). The drop in dissipation rates is slower after the contraction, which is consistent with earlier measurements, but one should also keep in mind the relatively low Re_λ for these experiments.

The scalar dissipation rate χ was obtained similarily by integrating $k_1^2 E_{\theta\theta}(k_1)$ and assuming isotropic relations. This may lead to significant underestimates of χ inside the contraction where the temperature field is far from isotropic as discussed in the previous section. Figure 28 shows the evolution of χ in the streamwise direction for both Δx. χ increases significantly downstream of the contraction when the flow readjusts after the release of the mean strain. The scalar dissipation rates for the weaker stratification grow even more strongly downstream of the contraction in accordance with the growth of the large scales (i.e. L_t), shown in figure 17. The evolution of the two dissipation rates is therefore qualitatively different.

4.12. *Length-scale evolution*

We now turn to the development of the different length scales defined in §2. The local values of N and $\mathrm{d}T/\mathrm{d}z$ are used in the definitions of many of these length scales. Since these quantities were not independently measured at most x locations, we used equation (3.1) to calculate $N(x)$. The local values of $\mathrm{d}T/\mathrm{d}z$ were similarily

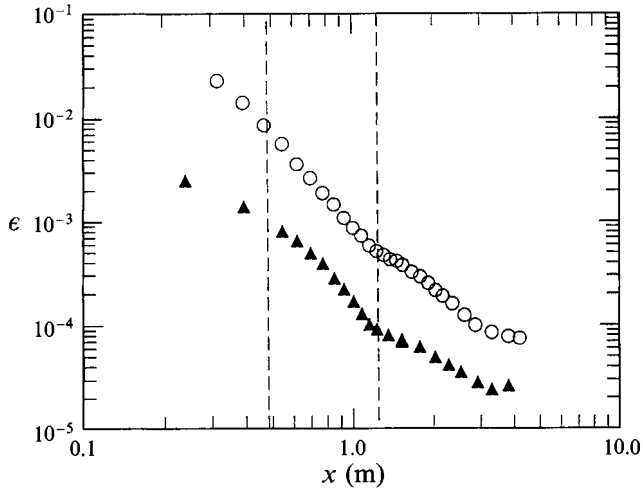

FIGURE 27. The kinetic energy dissipation rate *vs.* downstream location for $M = 5.08$ cm: open circles show results for $\Delta x = 48.3$ cm and the solid triangles for $\Delta x = 101.6$ cm. The vertical lines mark the locations of the contractions for the two cases; the results for $\Delta x = 101.6$ cm have been shifted in the x-direction so that the contraction exit coincides for the two cases.

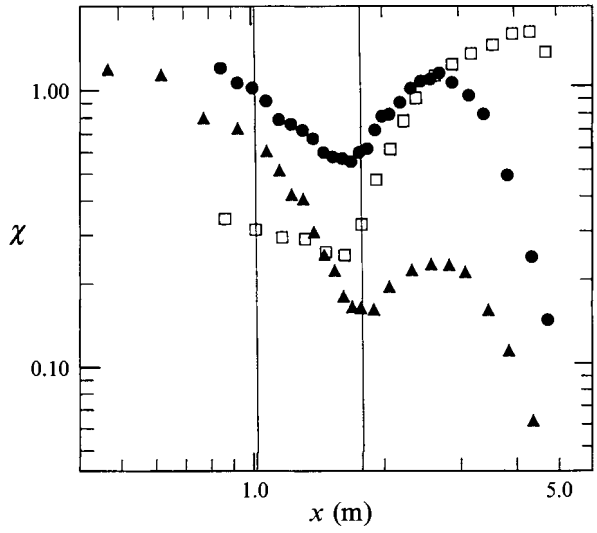

FIGURE 28. The scalar dissipation rates corresponding to the same conditions as figure 27. The results for $\Delta x = 101.6$ cm have been shifted to make the locations of the contraction the same for the two cases. The open squares show results for the passively stratified case, which have been multiplied by 10 to fit on the graph.

estimated according to the geometric relation

$$\frac{\mathrm{d}T}{\mathrm{d}z}(x) = \left(\frac{\mathrm{d}T}{\mathrm{d}z}\right)_1 \frac{U(x)}{U_1}.$$

Figures 29 and 30 show the evolution of the important length scales of buoyancy, overturning and viscous forces, for $\Delta x = 48$ and 102 cm respectively, for $N_2 = 2.22$ rad s^{-1} in both cases. Initially the evolution follows the well-known results for

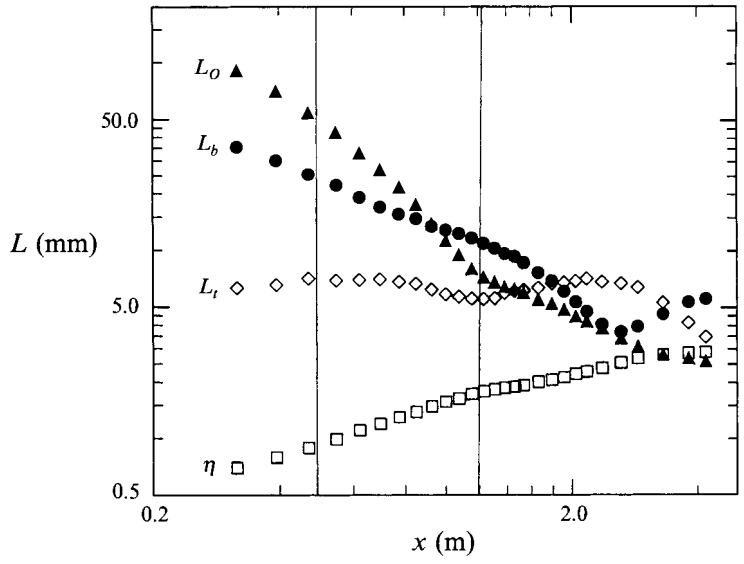

FIGURE 29. The evolution of the turbulent length scales through the contraction. ▲, L_O; ●, L_b; ◇, L_t; □, η. $\Delta x = 48.3$ cm, $M = 5.08$ cm. $N_2 = 2.22$ rad s^{-1}.

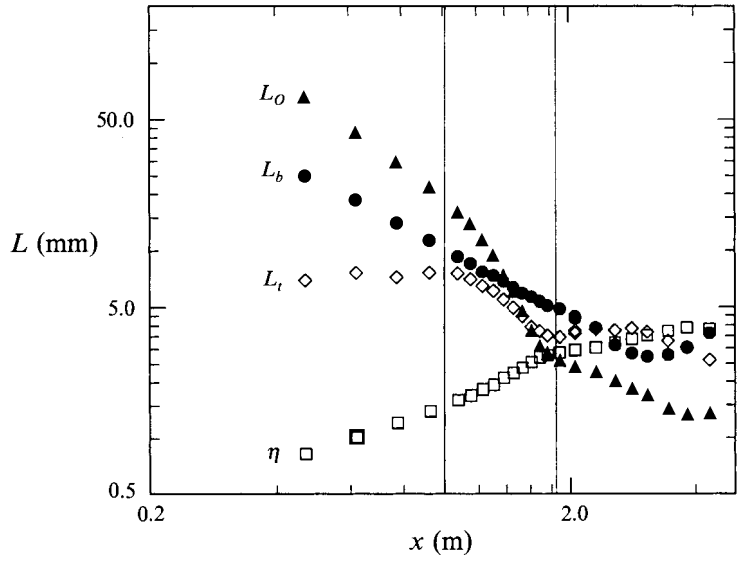

FIGURE 30. The evolution of the same length scales as figure 29, now for $\Delta x = 101.6$ cm, resulting in a smaller ratio of L_O over L_t as the turbulence enters the contraction. $M = 5.08$ cm. $N_2 = 2.22$ rad s^{-1}.

decaying turbulence, i.e. a decrease in L_b and growth of L_t as observed for example by Lienhard & Van Atta (1990) for the decaying case without a contraction. However, within and downstream of the contraction important differences are noticed, as L_t overtakes the buoyancy scale L_b and the two oscillate around a common mean. This is implicit from the energy results presented in §4.8.

The main dynamical difference between the evolution for the two values of Δx is the

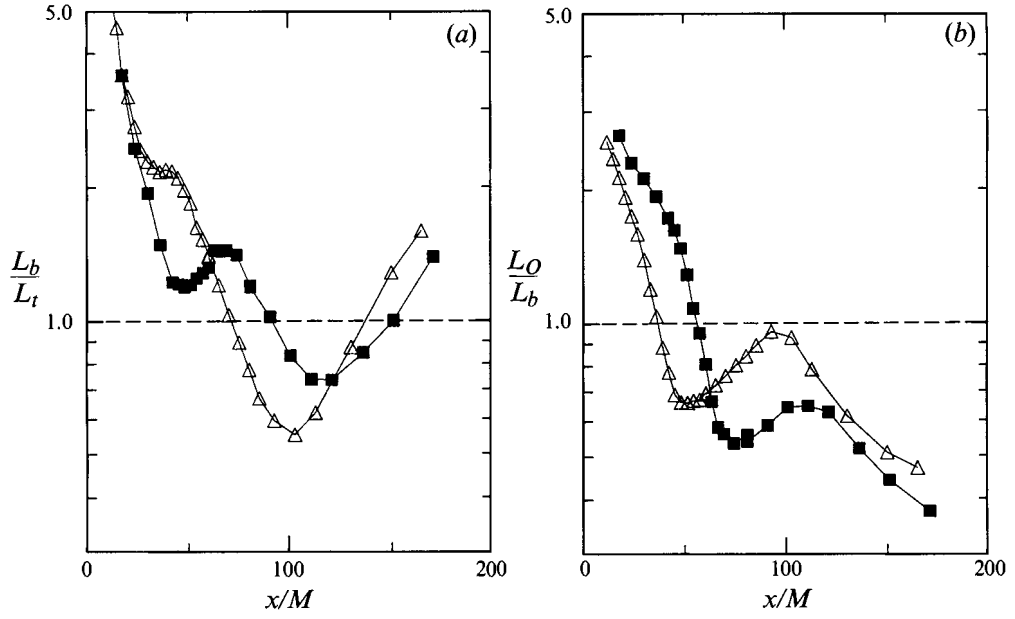

FIGURE 31. Ratio of buoyancy and turbulence length scales. (*a*) The ratio of L_b and L_t for the two Δx. (*b*) The ratio of L_O and L_b for the two Δx. Open triangles represent data for $\Delta x = 48.3$ cm, and filled squares for $\Delta x = 101.6$ cm.

difference in the ratio L_b/L_t as the turbulence enters the contraction. For the shorter Δx this ratio is 2.2 while for the larger one it takes the value of 1.2. The buoyancy forces are thus much more important for the $\Delta x = 102$ cm case. The downstream changes in this ratio are shown in figure 31(*a*) for both cases. It is significant that L_b becomes as small as half the size of L_t, especially since this ratio does not go significantly below unity for the decaying turbulence without a contraction (Lienhard & Van Atta 1990, figure 3). One should keep in mind the earlier discussion about the effect of anisotropy of the θ fluctuations on the estimation of L_t.

For the larger Δx the Kolmogorov length scale becomes of comparable size to the other length scales, further demonstrating the extinction of the turbulence and presence of fossil states. This clearly shows that viscous effects must be important in the dynamics. However, the buoyancy–inertial interactions seem to dominate the evolution judging from the very similar evolution for the two different mesh sizes studied.

There are also significant differences between the behaviour of L_b and L_O. This may be due to the breakdown of the relation $\epsilon \approx u^3/\ell$, which is used in the derivation of L_O. The ratio L_O/L_b is shown in figure 31(*b*). This ratio varies by an order of magnitude, falling significantly below one far downstream. This may partly be explained by the fact that L_O emphasizes small scales through ϵ, whereas L_b will contain contributions from internal waves.

5. Discussion and conclusions

5.1. *Comparison with the numerical simulations of Gerz & Yamazaki (1993)*

Gerz & Yamazaki (1993) have performed direct numerical simulations (DNS) of 'turbulence' arising from initial density fluctuations in a fluid at rest, having a

background stable linear mean density gradient. These DNS covered three different initial stratification numbers St as well as two values of the Prandtl number, i.e. Pr of 1 and 2. As elaborated earlier, our data show strong rejuvenation of 'turbulent' motion through restratification induced by the imposed increase in N. It therefore seems worthwhile to compare our results to a subset of the abovementioned simulations. There are however some practical difficulties associated with this comparison. First, the velocity fluctuations in our experiments never completely vanish and secondly the density field downstream of the contraction is not isotropic, as demonstrated in §4.10. These two factors make it difficult to determine an appropriate starting point of the comparison and stratification numbers for the experiments. Here we have selected to align the Nt- or x-axes, for this comparison, at the streamwise location where the buoyancy flux first crosses the zero line from mixing into restratification. This allows the DNS flow field to attain some velocity fluctuations as well as allowing the experimental field to be well past the physical extent of the contraction.

The stratification number is defined in (1.1). For its determination one needs an estimate of the integral scale of the density field. In the abovementioned DNS it was determined from the three-dimensional spectral density (Hinze 1975, pp. 279–285) as

$$\Lambda_\theta = \int_0^\infty R_{\theta,\theta}(r)\mathrm{d}r = \frac{\pi}{2\theta^2}\int_0^\infty \frac{E_\theta(k)}{k}\mathrm{d}k = \frac{\pi}{2\theta^2}E_{\theta 1}(0) \tag{5.1}$$

where $E_\theta(k)$ is the three-dimensional density spectra and $E_{\theta 1}(k)$ its one-dimensional counterpart obtained from measurements in the streamwise direction. Using this definition of Λ_θ we get a value for the stratification number of about 2 at the entrance to the contraction for the case of $\Delta x = 48.3$ cm and $N_2 = 2.22$ rad s^{-1}. Stratification numbers for stratified grid turbulence without a contraction calculated from the data of Thoroddsen & Van Atta (1992) are about 1 leaving the grid. Far downstream of the contraction there is a rapid rise in St in the final stage of the decay which may indicate a transition to internal waves, where Λ_θ will become very large. It is interesting to note that the contraction increases the stratification number, mostly due to the increase in $\mathrm{d}T/\mathrm{d}z$. When compared to decaying grid turbulence without a contraction the much weaker restratification, observed in that case, is consistent with the DNS results for $St = \frac{1}{4}$.

Based on the discussion in §4.10 it can be deduced that this value of St may be as much as 40% smaller if one uses Λ_z. We have therefore chosen to compare our results to the $St = 1$ case in the DNS. The DNS results for $St = 4$ are essentially the same, whereas for $St = 0.25$ the results are qualitatively different. Here we will only compare the evolution of the buoyancy flux. Figure 32 shows that there is close quantitative correspondence between our data and the DNS for the normalized flux values. The period of the fluctuations in the flux is somewhat different, but increases for both the simulations and the experiment.

The results for other quantities, such as temperature fluctuations, scalar dissipation and the hydrodynamic phase diagram (not shown here) are also qualitatively similar to those of Gerz & Yamazaki (1993) for the cases with the larger stratification numbers.

We conclude that the general flow development is thus in good agreement with the numerical simulations.

5.2. *Large-scale anisotropy inside the contraction*

Measurements of integral scales in contracting flows are scarce. The most relevant data available are those obtained by Mills & Corrsin (1959), for non-stratified passive

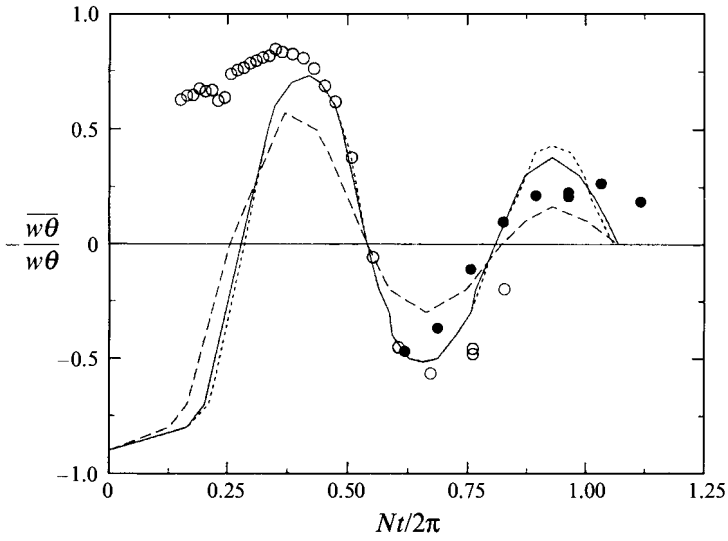

FIGURE 32. Comparison of normalized buoyancy flux results with the direct numerical simulations of Gerz & Yamazaki (1993). Their numerical cases correspond to initial St of 0.25 (- - - -), 1.0 (—-) and 4.0 (. . . .). The experimental data symbols correspond to those on figure 11.

scalar fluctuations as well as velocity fluctuations downstream of a 4 to 1 three-dimensional contraction. They observed qualitatively similar results to ours, for the ratio of the integral scales of velocity Λ_z/Λ_x. This ratio took a value of approximately 0.5 shortly after the contraction exit. Further downstream the ratio relaxes slowly to 0.6 at three contraction lengths downstream. The stronger effects of the strain, i.e. a smaller ratio, observed by these authors, compared to our results in figure 24, can be explained by their larger contraction ratio. Similarly for the integral scales of the temperature fluctuations they show a ratio Θ_z/Θ_x of 0.19 versus 0.34 farther downstream. Here again, direct comparison is difficult due to the difference in the contraction geometry and contraction ratio, as well as the mean scalar field structure. Also, for the temperature fluctuations comparison is made even more difficult due to the additional coupling between the vertical velocity fluctuations and the scalar field caused by the presence of the mean vertical scalar gradients, in our experiments. But qualitatively the Mills & Corrsin results are consistent with ours, in the relative large-scale anisotropy of the scalar field being more significant than that of the velocity field.

5.3. *Review of the main results*

We have studied the dynamics of stably stratified turbulence which is passed through a vertical contraction. The turbulence thus experiences a spatial variation in stratification strength, as well as a streamwise mean strain. In the passively stratified case the stretching of streamwise vortices enhances the vertical velocity fluctuation in the typical manner. However, for the strongly stratified case the increased strength of buoyancy forces inhibits this stretching-induced overturning at the large scales and fossilizes the density field, which subsequently leads to *zombie*-type revival of vertical motions. This shut-off of the large-scale overturns by buoyancy forces is demonstrated by the reduction in w', L_t and $E_{\theta\theta}(k_1)$ at the large scales, as well as by

comparison of $E_{ww}(k_1)$ for stratified and non-stratified experiments. The restratification starts at the large scales and is then observed to transfer energy down to smaller scales.

Some enhancement of normalized vertical heat flux is observed inside the contraction, but downstream of it, coinciding with the fossilization, the buoyancy flux collapses rapidly, subsequently producing much stronger restratification than has been observed in any previous experiments of decaying stratified turbulence. The normalized rate of decrease of the flux is more than twice as rapid as that observed in decaying stratified turbulence without a contraction. At the height of fossilization the vertical kinetic energy is reduced to only a quarter of the turbulent potential energy. The following restratification creates significant vertical velocity fluctuations. The lack of the corresponding increase in $E_{\theta\theta}(k)$ clearly shows that these w-fluctuations are generated by the movement of buoyant blobs and are not due to active turbulent overturns against the background mean temperature gradient.

The strongest rebounding in w' previously observed experimentally was that by Yoon & Warhaft (1990, p. 613), but their restratification normalized buoyancy flux values were much smaller (−0.21) than those observed here, which are as large as −0.55.

The lack of active overturning turbulence in the initial *zombie* region of the flow is in agreement with the numerical simulations of Gerz & Yamazaki (1993) for small stratification numbers.

The qualitative results were the same for both grid mesh sizes used, indicating that, despite the relatively low turbulence Reynolds numbers at the generating grid, Re_λ was large enough that the interactions through the contraction were governed more by inertial–buoyancy interactions than by viscous forces.

5.4. *Further work*

It is clear that passing stratified turbulence through a contraction leads to new non-equilibrium turbulent states, i.e. dynamical states that the conventional decaying grid turbulence will not evolve into of its own accord. Contraction configurations are therefore well suited for designing new experiments that can visit exotic regions of the hydrodynamic phase diagram. Such experiments are important in order to verify results from numerical simulations where those regions can be more easily visited. The main control parameters available to control these states are Δx, the distance from the grid to the contraction's entrance, and the contraction ratio.

It appears that the strongest restratification will occur by contracting the turbulence close to the grid, before buoyancy forces have become strong enough to begin prohibiting the overturns. This means imparting large kinetic energy and temperature fluctuations to the field just as it enters the contraction. Further experiments with larger contraction ratios than are practical with the current facility might prove interesting. Experiments with larger initial Reynolds numbers would also be valuable.

Expansion of the flow in the vertical direction might more be likely to succeed in generating lower St, primarily since an expansion will decrease $\mathrm{d}T/\mathrm{d}z$.

We acknowledge helpful discussions with Professor C. H. Gibson and H. Yamazaki. Work was supported by ONR Contract # N00014-94-1-0233 and NSF grant OCE92-17213.

REFERENCES

ARMI, L. & FARMER, D. M. 1986 Maximal two-layer exchange through a contraction with barotropic net flow. *J. Fluid Mech.* **164**, 27–51.

BATCHELOR, G. K., CANUTO, V. M. & CHASNOV, J. R. 1992 Homogeneous buoyancy-generated turbulence. *J. Fluid Mech.* **235**, 349–378.

BJERKNES, V. 1918 Vid-Selsk. Skrifter, Trondheim University Press.

BRITTER, R. E., HUNT, J. C. R., MARSH, G. L. & SNYDER, W. H. 1983 The effects of stable stratification on turbulent diffusion and the decay of grid turbulence. *J. Fluid Mech.* **127**, 27–44.

BROADWELL, J. E. & BREIDENTHAL, R. E. 1982 A simple model of mixing and chemical reaction in a turbulent shear layer. *J. Fluid Mech.* **125**, 397–410.

CHASNOV, J. R. 1991 Decaying turbulence in a uniform mean scalar gradient. *CTR Manuscript* 130.

DICKEY, T. D. & MELLOR, G. L. 1980 Decaying turbulence in neutral and stratified fluids. *J. Fluid Mech.* **99**, 13–31.

FARMER, D. M. & ARMI, L. 1986 Maximal two-layer exchange over a sill and through the combination of a sill and contraction with barotropic flow. *J. Fluid Mech.* **164**, 53–76.

GERZ, T. & YAMAZAKI, H. 1993 Direct numerical simulation of buoyancy-driven turbulence in stably stratified fluid. *J. Fluid Mech.* **249**, 415–440.

GIBSON, C. H. 1980 Fossil temperature, salinity, and vorticity turbulence in the ocean. In *Marine Turbulence*, pp. 221–257. Elsevier.

GIBSON, C. H. 1991 Laboratory, numerical and oceanic fossil turbulence in rotating and stratified flows. *J. Geophys. Res.* **96**, C7, 12549–12566.

HINZE, J. O. 1975 *Turbulence.* McGraw-Hill.

ITSWEIRE, E. C., HELLAND, K. N. & VAN ATTA, C. W. 1986 The evolution of grid-generated turbulence in a stably stratified fluid. *J. Fluid Mech.* **162**, 299–338.

IVEY, G. N. & IMBERGER, J. 1991 On the nature of turbulence in a stratified fluid. 1. The energetics of mixing. *J. Phys. Oceanogr.* **21**, 650–658.

LIENHARD V, J. H. & VAN ATTA, C. W. 1989 Thermally stratifying a wind tunnel for buoyancy influenced flows. *Exps. Fluids* **7**, 542–546.

LIENHARD V, J. H. & VAN ATTA, C. W. 1990 The decay of turbulence in thermally stratified flow. *J. Fluid Mech.* **210**, 57–112.

LIN, J. T. & VEENHUIZEN, S. D. 1975 Measurements of the decay of grid-generated turbulence in a stratified fluid. *Flow Research Note* 85.

MÉTAIS, O. & HERRING, J. R. 1989 Numerical simulations of freely evolving turbulence in stably stratified fluids. *J. Fluid Mech.* **202**, 117–148.

MILLS, R. R. & CORRSIN, S. 1959 Effect of contraction on turbulence and temperature fluctuations generated by a warm grid. *NASA MEMO* 5-5-59W.

MILLS, R. R., KISTLER, A. L., O'BRIEN, V. & CORRSIN, S. 1958 Turbulence and temperature fluctuations behind a heated grid. *NACA Tech. Note* 4288.

OZMIDOV, R. V. 1965 On the turbulent exchange in a stably stratified ocean. *Izv. Acad. Sci. USSR Atmos. Ocean. Phys.* (English Transl.) **1**(8), 853–860.

PRANDTL, L. 1933 Attaining a steady air stream in wind unnels. *NACA TM* 726.

ROHR, J. J., ITSWEIRE, E. C., HELLAND, K. N. & VAN ATTA, C. W. 1988 Growth and decay of turbulence in a stratified shear flow. *J. Fluid Mech.* **195**, 77–111.

SCOTTI, R. S. & CORCOS, G. M. 1972 An experiment on the stability of small disturbances in a stratified free shear layer. *J. Fluid Mech.* **52**, 499–528.

STILLINGER, D. C., HELLAND, K. N. & VAN ATTA, C. W. 1983 Experiments on the transition of homogeneous turbulence to internal waves in a stratified fluid. *J. Fluid Mech.* **131**, 91–122.

TAYLOR, G. I. 1935 Statistical theory of turbulence, Part I. *Proc. R. Soc. Lond.* A **151**, 421–444.

TENNEKES, H. & LUMLEY, J. L. 1972 *A First Course in Turbulence.* MIT Press.

TOWNSEND, A. A. 1954 The uniform distortion of homogeneous turbulence. *Q. J. Mech. Appl. Maths* **7**, 704–727.

THORODDSEN, S. T. & VAN ATTA, C. W. 1992 The influence of stable stratification on small-scale anisotropy and dissipation in turbulence. *J. Geophys. Res.* **97**,C3, 3647–3658.

THORODDSEN, S. T. & VAN ATTA, C. W. 1993*a* Experimental study of the effects of grid configuration on stably stratified grid-turbulence. *Dyn. Atmos. Oceans* **19**, 259–288.

THORODDSEN, S. T. & VAN ATTA, C. W. 1993*b* Experiments on density-gradient anisotropies and scalar dissipation in stably stratified turbulence. *UCSD Manuscript.*

TURNER, J. S. 1973 *Buoyancy Effects in Fluids.* Cambridge University Press. WARHAFT, Z. 1980 An experimental study of the effect of uniform strain on thermal fluctuations in grid-generated turbulence. *J. Fluid Mech.* **99**, 545–573.

WARHAFT, Z. 1980 An experimental study of the effect of uniform strain on thermal fluctuations in grid-generated turbulence. *J. Fluid Mech.* **99**, 545–573.

WARHAFT, Z. & LUMLEY, J. L. 1978 An experimental study of the decay of temperature fluctuations in grid-generated turbulence. *J. Fluid Mech.* **88**, 659–684.

YEH, T. T. & VAN ATTA, C. W. 1973 Spectral transfer of scalar and velocity fields in heated-grid turbulence. *J. Fluid Mech.* **58**, 233–261.

YOON, K. & WARHAFT, Z. 1990 The evolution of grid generated turbulence under conditions of stable thermal stratification. *J. Fluid Mech.* **215**, 601–638.